

Air Force Institute of Technology AFIT Scholar

Theses and Dissertations

Student Graduate Works

3-11-2011

Simulating the Effects of an Extended Source on the Shack-Hartmann Wavefront Sensor through Turbulence

Jeffery S. Dennison

Follow this and additional works at: <https://scholar.afit.edu/etd>

Part of the [Optics Commons](#)

Recommended Citation

Dennison, Jeffery S., "Simulating the Effects of an Extended Source on the Shack-Hartmann Wavefront Sensor through Turbulence" (2011). *Theses and Dissertations*. 1377.
<https://scholar.afit.edu/etd/1377>

This Thesis is brought to you for free and open access by the Student Graduate Works at AFIT Scholar. It has been accepted for inclusion in Theses and Dissertations by an authorized administrator of AFIT Scholar. For more information, please contact richard.mansfield@afit.edu.



**SIMULATING THE EFFECTS OF AN
EXTENDED SOURCE ON THE
SHACK-HARTMANN WAVEFRONT SENSOR
THROUGH TURBULENCE**

THESIS

Jeffery Dennison, Captain, USAF
AFIT/GE/ENG/11-08

**DEPARTMENT OF THE AIR FORCE
AIR UNIVERSITY**

AIR FORCE INSTITUTE OF TECHNOLOGY

Wright-Patterson Air Force Base, Ohio

APPROVED FOR PUBLIC RELEASE; DISTRIBUTION UNLIMITED.

The views expressed in this thesis are those of the author and do not reflect the official policy or position of the United States Air Force, Department of Defense, or the United States Government. This material is declared a work of the U.S. Government and is not subject to copyright protection in the United States.

AFIT/GE/ENG/11-08

SIMULATING THE EFFECTS OF AN EXTENDED SOURCE ON THE
SHACK-HARTMANN WAVEFRONT SENSOR THROUGH TURBULENCE

THESIS

Presented to the Faculty
Department of Electrical and Computer Engineering
Graduate School of Engineering and Management
Air Force Institute of Technology
Air University
Air Education and Training Command
in Partial Fulfillment of the Requirements for the
Degree of Master of Science in Electrical Engineering

Jeffery Dennison, BSEE
Captain, USAF

March 2011

APPROVED FOR PUBLIC RELEASE; DISTRIBUTION UNLIMITED.

SIMULATING THE EFFECTS OF AN EXTENDED SOURCE ON THE
SHACK-HARTMANN WAVEFRONT SENSOR THROUGH TURBULENCE

Jeffery Dennison, BSEE
Captain, USAF

Approved:

//signed//

March 2011

Jason D. Schmidt (Chairman)

Date

//signed//

March 2011

Salvatore J. Cusumano (Member)

Date

//signed//

March 2011

Michael R. Hawks (Member)

Date

Abstract

Perspective elongation in Shack-Hartmann wavefront sensor (SHWFS) spots is a phenomenon caused by an extended three-dimensional scattering beacon in the mesosphere (80-100km). Elongated spots cause errors in wavefront sensor measurements, which leads to poor turbulence compensation and decreased image resolution of the optical system. In order to compensate for elongated spots, a proper beacon model must be developed to simulate the error. In this paper, a documented theory for modeling an elongated sodium beacon and elongated SHWFS spots using sodium layer “slices” was tested. It was found that nine evenly-spaced slices were adequate to model the elongated beacon in the most stringent, turbulence-included case. Furthermore a bench-top source was developed and tested to model SHWFS spot elongation in the lab. The source demonstrated the principle theory, but requires a more robust design to simulate sodium layer depth. Being the first documented experiment using an extended source on an adaptive optics (AO) system, it enables further research on the effects of deep turbulence on AO systems and correlation based wavefront sensing with extended sources.

*I dedicate this work to my father, whose successful battle with cancer this year
inspired my to see this through.*

Acknowledgements

I have several people to thank, and, while I may not always show appreciation the way I should, I hope these people understand how truly helpful and supportive they were throughout my research. First, I owe a ton of gratitude to Maj Schmidt who was always available to take any of my questions (there were a lot). His knowledge, expertise, patience, and dedication is above and beyond any professor I have ever had, he is truly an asset to AFIT and the optics community. Next, I'd like to thank my committee members Dr. Salvatore Cusumano and Lt Col Michael Hawks for dedicating their time to supporting my research and keeping me on the right track. I would like to thank the OPTECS research group for sitting through my briefings and inspiring me to work hard. Also, a special thanks goes out to FLTLT Russell McGuigan. We shared classes, labs, and lots of frustration during our journey through the rigorous AFIT curriculum. Last, but not least, I would like to thank my wife who sacrificed as much as I did to assure my success in academia.

Jeffery Dennison

Table of Contents

	Page
Abstract	iv
Acknowledgements	vi
List of Figures	ix
List of Tables	xii
List of Abbreviations	xiii
I. Introduction	1
1.1 Objectives	2
1.2 Thesis Overview	3
II. Background and Related Research	5
2.1 Fourier Optics	5
2.1.1 Light as a Wave	5
2.1.2 Diffraction Imaging as a Linear Systems	7
2.2 Coherence Properties of Light	7
2.2.1 Spatial and Temporal Coherence	8
2.2.2 Diffusers	8
2.3 Sampling Theory	9
2.4 Atmospheric Distortion of Light	11
2.4.1 Atmospheric Turbulence	12
2.4.2 Atmospheric Condition Characterizations	15
2.5 Conventional Adaptive Optics	18
2.5.1 AO Basics	18
2.5.2 Starfire Optical Range	20
2.6 Shack-Hartmann Wavefront Sensor	22
2.6.1 History and Development	22
2.6.2 Principles of Operation	23
2.6.3 Perspective Elongation	27
2.7 Gaussian Beams	27
2.8 Laser Guide Stars and Sodium Layer Properties	30
2.9 Imagery Comparison Techniques	33
2.9.1 Root Mean Square Error	33
2.9.2 Correlation	33
2.10 Chapter Summary	34

	Page
III. Research Methodology	35
3.1 Computer Simulation Environment	35
3.1.1 Grid Sampling	38
3.1.2 Atmospheric Characteristics and Verification	38
3.1.3 LGS Beam System Parameters	44
3.1.4 Simulating Perspective Elongation	47
3.2 Laboratory Description	51
3.2.1 AFIT AO Lab	51
3.2.2 ZEMAX Model	53
3.3 Extended Source Model Progression	55
3.3.1 Iris and Diffuser	56
3.3.2 System Magnification	58
3.3.3 Three-Dimensional Extended Source	58
3.4 Data Collection and Comparison	60
3.5 Chapter Summary	61
IV. Results and Analysis	63
4.1 Computer Simulation Results	63
4.1.1 RMS Percent Difference	63
4.1.2 Correlation Coefficient	64
4.2 Experimental Results	65
4.2.1 Iris and Diffuser	66
4.2.2 Three-Dimensional Extended Source	66
4.3 Chapter Summary	68
V. Conclusions and Recommendations	71
5.1 Summary	71
5.2 Novel Contributions	72
5.3 Recommendations	73
5.4 Chapter Summary	77
A. MATLAB Code	78
Bibliography	87

List of Figures

Figure		Page
2.	Geometric vs Fourier optics	6
3.	Linear Optical Systems	8
4.	Aliasing	10
5.	Wavefront distortion due to turbulence	12
6.	PSD model comparison	14
7.	Coherence Length	16
8.	Isoplanatic Angle	17
9.	Basic AO system	19
10.	Closed-loop vs Open-loop	20
11.	SOR 3.5 meter telescope	21
12.	The binary star system k-Peg	22
13.	Hartmann screen and lenslet array	23
14.	Basic SHWFS diagram	24
15.	Quad-cell detector	25
16.	SHWFS lenslet geometry	26
17.	Perspective elongation example	28
18.	Perspective elongation from elongated beacon	31
19.	Column density of the sodium layer	32
20.	Software model geometry	36
21.	Sodium layer slices	37
22.	Sampling analysis	39
23.	Kolmogorov phase screen	41

Figure	Page
24.	Structure function - one phase screen 42
25.	Structure function - 3D turbulence model 42
26.	Log amplitude PDF 43
27.	MSE to find Rytov number 44
28.	Spot size trend 45
29.	Gaussian beam vac propagation: WaveProp vs theory 46
30.	Gaussian beam turb propagation: WaveProp vs theory 47
31.	Beacon shapes at 90km 48
32.	Point source coordinates 49
33.	Elongated SHWFS spots 50
34.	AFIT lab bench-top layout 52
35.	ZEMAX model of AFIT lab bench-top 54
36.	Transverse magnification 55
37.	Spinning diffuser and iris 57
38.	Diffuser effects 57
39.	SHWFS spots from a 1mm source 59
40.	Spinning diffuser and rotated iris 60
41.	Rotated iris geometry 61
42.	RMS percent difference 64
43.	Correlation coefficient 65
44.	Elongated source and SHWFS spots (vacuum) 69
45.	Elongated beacons and SHWFS spots (turbulence) 70
46.	Sodium layer slicing methods 74

Figure		Page
47.	Rice grain and reflector tube	76
48.	LED bar	76

List of Tables

Table		Page
1.	Sampling parameters	38
2.	Atmospheric parameters	40
3.	Gaussian beam parameters: seven slices scenario	45
4.	Point source coordinates	49
5.	Lab bench components	52
6.	Sensor settings for data collection	61
7.	Iris and Diffusers	66

List of Abbreviations

Abbreviation		Page
AO	adaptive optics.....	1
NGAS	Sodium Guidestar AO for Space Situational Awareness.....	1
SOR	Starfire Optical Range	1
SHWFS	Shack-Hartmann wavefront sensor	1
FSM	fast-steering mirror	1
DM	deformable mirror	1
LGS	laser guide star	2
PSF	point spread function	7
ISO	International Organization for Standardization	9
PSD	power spectral density	13
MTF	mutual transfer function	15
WFS	wavefront sensor	19
USAF	United States Air Force	22
OSC	Optical Science Center	22
RMS	root mean square.....	33
ATS	atmospheric turbulence simulator.....	51
ROI	region of interest	67
SRI	self-referencing interferometer	72
LED	light emitting diode	75

SIMULATING THE EFFECTS OF AN EXTENDED SOURCE ON THE SHACK-HARTMANN WAVEFRONT SENSOR THROUGH TURBULENCE

I. Introduction

The Air Force Research Laboratory's Sodium Guidestar Adaptive Optics (AO) for Space Situational Awareness program (NGAS) at the Starfire Optical Range (SOR) at Kirtland Air Force Base has sponsored research on non-uniform spot analysis in Shack-Hartmann wavefront sensor (SHWFS) subapertures. The SHWFS is used to measure incoming wavefront slopes by measuring the centroid displacement of focused spots. When the spots are not uniform, errors in slope measurements occur which decreases the resolution of the optical system. Researching how to reproduce and account for non-uniform spots will push the system to the diffraction limit, and lead to higher resolution imagery of intended targets.

AO is a technology for sensing and correcting dynamic wavefront distortions in real time. Often, it is used to correct for optical fluctuations due to atmospheric turbulence and improve imaging system performance. Common elements in an AO system include a fast-steering mirror (FSM), deformable mirror (DM), and a wavefront sensor. These elements are connected in a feedback, control loop enabling them to communicate and compensate in real-time.

AO systems require a light source or beacon to measure the wavefront. Ideal beacons are natural stars which, when available, work very well[1]. Natural stars with the requisite brightness are not available in every part of the sky, however. For the 3.5m telescope at the SOR, a 6th visual magnitude star or brighter is needed for high-order AO. There are only a few stars per degree of sky coverage with the

requisite brightness for AO. At a wavelength of 500nm, the probability of finding a bright enough reference star nearby is about 7×10^{-7} [2]. To overcome this limitation, artificial stars created by lasers mounted on or near telescope apertures are used to create backscatter in the atmosphere. Typically called laser guide stars (LGS), these beacons enable imaging of object almost anywhere in sky. Several types of LGS's exist, but this research focuses on sodium LGS's since they are used at SOR and many other cutting-edge astronomical telescopes.

In the past decade, observatories like SOR, Keck, and others have begun relying on sodium LGS's as a wavefront reference source[3, 4]. Sodium LGS's excite atoms in the mesosphere, and the resultant resonant backscatter acts as a beacon which the telescope's AO system uses to sense and compensate for atmospheric turbulence. As an integral part of the AO system at SOR, the SHWFS is vital in calculating aberrated wavefront slopes. Any errors occurring within this device causes miscalculations in wavefront slopes and, inevitably, lower-resolution imagery. This research focuses on one such error: perspective elongation in SHWFS spots. This research does not attempt to correct this error, but accurately simulate it in wave propagation software and on a bench-top laboratory system. Models developed here be an important tool for researchers who seek to overcome perspective elongation and thereby produce high-resolution imagery.

1.1 Objectives

AO systems require the sodium beacon to be a point source to accurately measure the wavefront, which is one reason why natural stars are desirable. Unfortunately, due to diffraction, the depth of the sodium layer, imperfect beam quality, and the atmosphere, the beacon scatters from a large column and appears elongated when viewed by SHWFS subapertures. Furthermore, images of the SHWFS spots are elongated

differently based on each subaperture’s viewing angle relative to the beacon scattering spot [5, 6]. This phenomenon is typically referred to as perspective elongation. The goal of this research is to explore mitigating solutions for reproducing perspective elongation in SHWFS subapertures in a lab setting. Specifically, the objectives include:

1. test a current, accepted method used to simulate a three-dimensional scattering volume in the sodium layer with wave propagation software,
2. quantitatively determine the required number of sodium layer slices needed to accurately simulate an elongated beacon,
3. create and implement the first optically designed bench-top method of producing coherent, extended sources,
4. use the coherent, extended sources to produce elongation in a SHWFS, and
5. deliver a working, scalable model for simulating perspective elongation in wave propagation software, and deliver a foundation for producing elongation in an optics laboratory.

Each of these goals were achieved with acceptable results. The analysis in the research evaluated the number of sodium layer slices to sufficiently model an elongated sodium beacon. The result is consistent with Viard’s seven-slice model[5]. A spinning diffuser and adjustable iris were illuminated by a laser to create an incoherent, extended source. Imaging the source with the SHWFS produced elongated spots.

1.2 Thesis Overview

Chapter II provides an introduction to Fourier optics, Gaussian laser beam propagation, sodium layer properties, and atmospheric turbulence. Additionally, conven-

tional AO systems are discussed including an in-depth description of the SHWFS and the telescope at SOR. In Chapter III, a proposed method to simulate perspective elongation using wave propagation software is tested. Also, the methodology for simulating perspective elongation in a bench-top experiment is outlined. Chapter IV analyzes the results of the software simulations and lab experiments, and determines the most accurate way to simulate perspective elongation. Finally, Ch. V summarizes the research presented here and highlights key results and contributions to science. Additionally, it discusses ideas for future work to further the research on perspective elongation.

II. Background and Related Research

This chapter introduces some basic concepts in the field of optics. First, some principles of Fourier optics are briefly discussed. Next, methods for modeling atmospheric turbulence are described. Then, sampling theory for numerical wave propagation simulations is given. Modern AO systems are outlined, including a look at the system used at SOR, and the theory behind the Shack-Hartmann wavefront sensor. Finally, mathematical models for Gaussian beams are given along with characteristics of the sodium layer and the concept of laser guide stars. This information provides the background necessary to effectively model perspective elongation.

2.1 Fourier Optics

This section introduces some basic concepts of Fourier optics, which is a framework for describing optical diffraction phenomena using linear systems theory. Methods of modeling light propagation as a wave are introduced, and diffraction integrals are given. Then, the effect of lenses are described with application to imaging systems.

2.1.1 Light as a Wave.

Fourier optics is the science of propagating light through various media. It differs from geometrical optics in that it models light as electromagnetic waves instead of rays, which accurately accounts for diffraction effects. Figure 2 shows the basic difference between geometric and Fourier optics by showing how a plane wave propagates through a focusing lens. In geometric optics, the rays are focused to a sharp point on the screen, while in Fourier optics the wave is focused to a Bessel function[7].

When a light source is propagated through space, its field in the observation plane is found by numerically evaluating the Fresnel integral. The generalized expression,

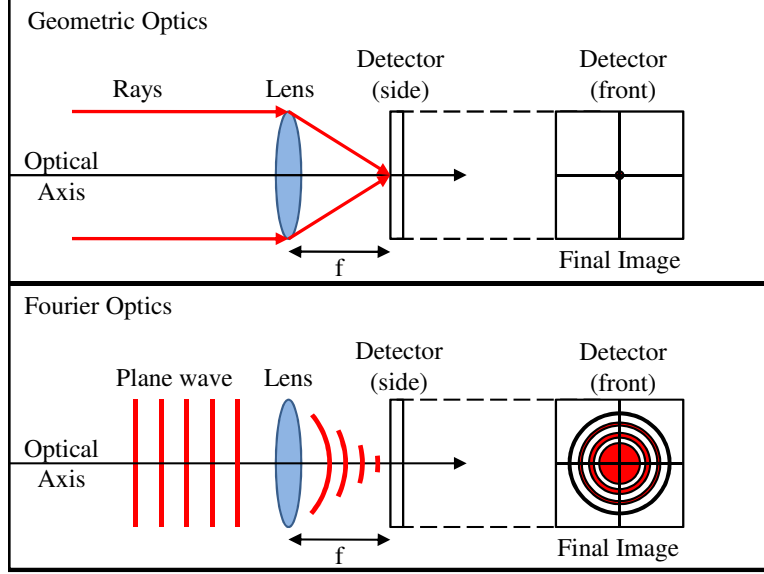


Figure 2. In the geometric optics model (top) the plane wave is focused to a perfect point by the lens. In the Fourier optics model (bottom) the plane wave is focused to a Bessel function due to the shape of the lens and diffraction effects.

with the applied paraxial approximation, is given by:

$$U(x_2, y_2) = \frac{e^{jkz}}{j\lambda\Delta z} \int_{-\infty}^{\infty} \int_{-\infty}^{\infty} U(x_1, y_1) e^{j\frac{k}{2\Delta z}[(x_2-x_1)^2+(y_2-y_1)^2]} dx_1 dy_1, \quad (1)$$

where x_1, y_1 are coordinates in the source plane, x_2, y_2 are coordinates in the observation plane, and z is the propagation distance[7]. By expanding and rearranging the terms in the exponent, Eq. (1) can be written as:

$$U(x_2, y_2) = \frac{e^{jkz}}{j\lambda\Delta z} e^{j\frac{k}{2\Delta z}(x_2^2+y_2^2)} \times \int_{-\infty}^{\infty} \int_{-\infty}^{\infty} U(x_1, y_1) e^{j\frac{k}{2\Delta z}(x_1^2+y_1^2)} e^{-j\frac{2\pi}{\lambda\Delta z}(x_2x_1+y_2y_1)}. \quad (2)$$

When the propagation distance Δz is “very far” the quadratic phase has such a large radius of curvature that it can be considered nearly flat for small viewing angles. In

this case, Eq. (2) can be further simplified to the Fraunhofer integral given by:

$$U(x_2, y_2) = \frac{e^{jkz}}{j\lambda\Delta z} \int_{-\infty}^{\infty} \int_{-\infty}^{\infty} U(x_1, y_1) e^{j\frac{k}{2\Delta z}(x_1x_2+y_1y_2)} dx_1 dy_1. \quad (3)$$

With the simplification of the exponential term in the integral, this form is much easier to work with. To use the Fraunhofer integral, the propagation distance must satisfy the inequality:

$$\Delta z > \frac{2D^2}{\lambda}, \quad (4)$$

where D is the source diameter. All simulated propagations modeled in this research require the Fresnel integral due to the relatively short propagation distances.

2.1.2 Diffraction Imaging as a Linear Systems.

Determining the image of an object after propagation through an optical system can be done using principles of linear systems. A point source propagated from the source plane, through the optical system, forms a point spread function (PSF) at the observation plane. The point source can be thought of as the Greens function and the PSF the spatial impulse response of the system. Convolution of the PSF with the original image in the source plane forms the final image[7]. Figure 3 shows a depiction of this. This linear system approach to imaging each beacon layer is used in Ch. III to obtain SHWFS lenslet images

2.2 Coherence Properties of Light

This section discusses the differences between coherent and incoherent quasi-monochromatic light sources. The first section defines Spatial and Temporal coherence properties. In the second section, diffusers and the theory of transforming coherent sources into incoherent ones is outlined.

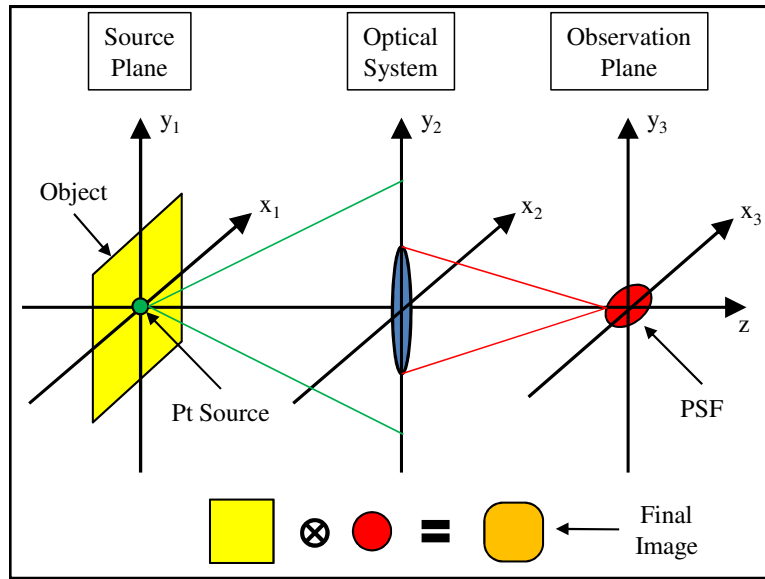


Figure 3. Imaging an object through an optical system done by propagating a point source (green) through the system and convolving the resultant PSF (red) with the original object (yellow) to get the final image (orange).

2.2.1 Spatial and Temporal Coherence.

Coherent properties are basically measures of how well parts of electromagnetic waves are related to one another. Every light source can be defined as spatially coherent, temporally coherent, both, or neither (completely incoherent). Spatial coherence is a measure of how well physical areas of a wavefront are correlated. Temporal coherence is a measure of how quickly two or more wave phases drift in and out of sync with each other. Faster drift means shorter coherence time, while slower drift means longer coherence time. As discussed further in Ch. III, experiments done in this research only consider spatial coherence properties of the source since temporal coherence properties don't have much effect.

2.2.2 Diffusers.

A diffuser is an optical component made of ground glass or a rough, reflective surface. Typically, they are used to scatter light to turn a spatially-coherent source

into a spatially-incoherent one. Diffusers are normally characterized by grit size and pupil size. The four standard commercial grit sizes, from coarsest to smoothest, have designations P120, P220, P600, and P1500 as defined by the International Organization for Standardization (ISO). The grit designations have average particle diameters of 125 microns, 68 microns, 25.8 microns, and 12.6 microns, respectively.

When a quasi-monochromatic laser is propagated through a stationary diffuser, an unwanted phenomenon known as speckle occurs. Speckle is a result of the interference of multiple waves, each with a different, random phase[8]. The addition of the waves causes random constructive and destructive interference patterns resulting in random intensities in the image plane. Even with speckle, the spatial coherence of the laser is still intact. A common way to remove speckle, and the spatial coherence, is by moving the diffuser[9] while propagating the light through it. This basically averages several random draws of the speckle intensity pattern in the image plane into a single, constant pattern.

2.3 Sampling Theory

When performing simulated propagations of waves, it is important to make sure the field is sampled correctly. An example of unacceptable wave sampling can be seen Fig. 4 where the "chirp" function (blue) is undersampled (black). The "chirp" function is, coincidentally, the real part of the Fresnel integral's quadratic phase discussed in Sec. 2.1. The wave continues to increase in frequency but the sampling criteria remains constant. In the beginning the sampling is fine, but as time increases the wave is very undersampled, with several wavelengths happening between each data point. This is called aliasing and must be avoided to properly propagate waves. Typically, one would apply the Nyquist criterion $\delta = 1/2f_{max}$ where f_{max} is the maximum spatial frequency of interest.

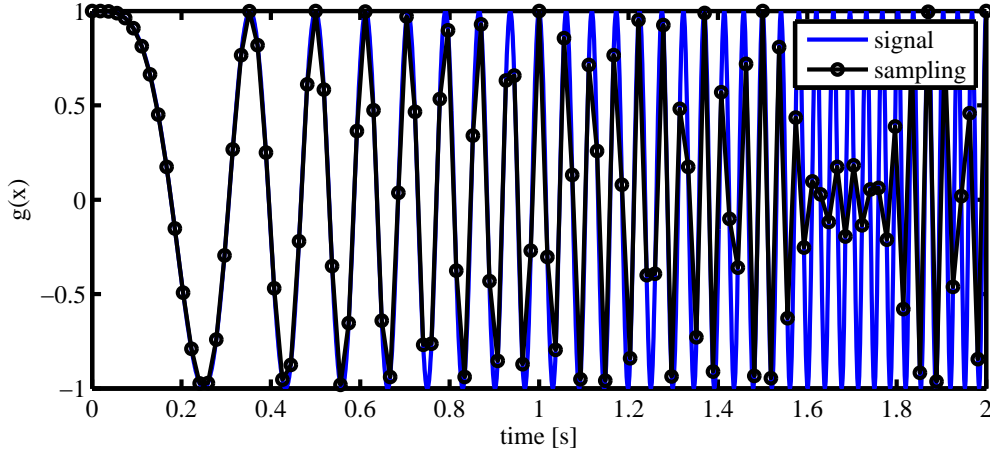


Figure 4. A chirp function (blue) with sampling (black). Aliasing is observed after 1 second because the frequency of the signal increases faster than the sampling.

Following Schmidt's method for wave propagation outlined in [10], three sampling parameters must be calculated: grid size N , grid spacing in the source plane δ_1 , and the grid spacing in the observation plane δ_n . These values are dependent on each other, and determined by the following 4 constraints:

1. $\delta_n \leq \frac{\lambda z - D_n \delta_1}{D_1}$
2. $N \geq \frac{D_1}{2\delta_1} + \frac{D_n}{2\delta_n} + \frac{\lambda \Delta z}{2\delta_1 \delta_n}$
3. $(1 + \frac{\Delta z}{R}) \delta_1 - \frac{\lambda \Delta z}{D_1} \leq \delta_n \leq (1 + \frac{\Delta z}{R}) \delta_1 + \frac{\lambda \Delta z}{D_1}$
4. $N \geq \frac{\lambda \Delta z_i}{\delta_1 \delta_n}$,

where D_1 is the diameter of the object at the source plane, D_n is the diameter of the object at the observation plane, λ is the wavelength, R is the radius of curvature, z is the total propagation distance, and Δz_i is the minimum, partial propagation distance. Since D_1 , D_2 , λ , z , and R are typically known parameters, the first three inequalities can be used to determine preliminary sampling values for N , δ_1 , and δ_n .

With the preliminary sampling requirements, the minimum propagation distance Δz_i and the number of propagations n can be determined. While dividing the total propagation distance z into several smaller propagation distance is not necessary, it greatly reduces the sampling constraint on N [10]. This enables use of a relatively

smaller grid size which greatly reduces simulation time. Finally, the total number of propagations is simply determined by $n = \text{ceil}(z/\Delta z_i) + 1$, where *ceil* is a MATLAB function that always rounds a fractional value to the next highest integer. It should be noted that this is the minimum number of propagations needed, shorter partial-propagation distances will still satisfy the fourth inequality. These sampling constraints are applied to all simulations as outlined in Ch. III.

2.4 Atmospheric Distortion of Light

The three atmospheric processes that affect optical wave propagation are absorption, scattering, and fluctuations in the refractive index[11]. Absorption and scattering mainly cause optical wave attenuation while index of refraction fluctuations cause irradiance fluctuations and loss of spatial coherence. This research assumes absorption and scattering effects are negligible, but takes into account the random, turbulent refractive index fluctuations. The theory is described here.

Due to the heating and cooling of the Earth's surface, large scale inhomogeneities in air temperature arise in the atmosphere. These inhomogeneities naturally breakdown into smaller and smaller pockets. The small, randomly-evolving pockets are typically called eddies. Each eddie in turn acts as tiny lens with an refractive index that slightly varies from the mean value of 1. As light propagates from distant objects in space through the atmosphere, its path is altered and it accumulates random phase due to these eddies. This leads to irradiance fluctuations and loss of spatial coherence in the wavefront. One can witness this in the form of twinkling stars in the night sky. Figure 5 shows a graphic of a wavefront after it passes through the atmosphere. AO systems attempt to correct these distorted wavefronts to their ideal form, so it is necessary to effectively model turbulence before designing an AO system.

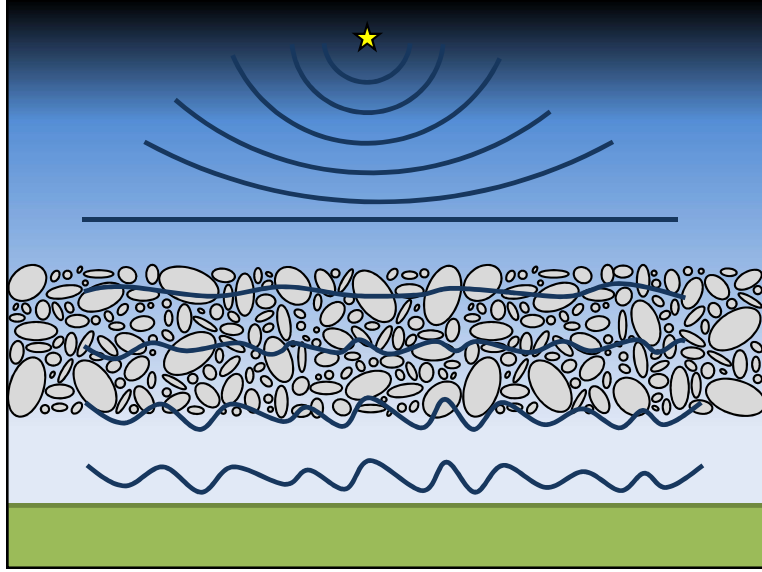


Figure 5. The wavefront from a distant object is nearly planar when it reaches the Earth’s atmosphere. As the wavefront passes through the turbulence (gray), it becomes more perturbed.

2.4.1 Atmospheric Turbulence.

Analytically modeling turbulent flow is challenging, but a common approach involves statistical methods. One such method is Kolmogorov turbulence theory which exploits the fact that small-scale structures in turbulent air flow are statistically isotropic for large Reynolds numbers (Reynolds numbers being the measure of the ratio of inertial forces to viscous forces)[11]. Due to its sensitivity to temperature variations, the atmosphere’s index of refraction $n(\mathbf{R}, t)$ can be expressed as

$$n(\mathbf{R}, t) = n_0 + n_1(\mathbf{R}, t), \quad (5)$$

where n_0 is the mean value of the index of refraction and $n_1(\mathbf{R}, t)$ is a random deviation from the mean at spatial coordinates \mathbf{R} and time t [12]. Normally, the mean value n_0 is 1 and time variations are suppressed in optical wave propagations, reducing Eq. (5) to

$$n(\mathbf{R}) = 1 + n_1(\mathbf{R}). \quad (6)$$

The deviations in the index of refraction are related to corresponding temperature $T(\mathbf{R})$ and pressure $P(\mathbf{R})$ fluctuations. For visible and infrared (IR) wavelengths they are expressed by

$$n_1(\mathbf{R}) = 7.76 \times 10^{-5} (1 + 7.52 \times 10^{-3} \lambda^{-2}) \frac{P(\mathbf{R})}{T(\mathbf{R})}. \quad (7)$$

For a wavelength of 500nm, Eq. 7 becomes:

$$n(\mathbf{R}) = 1 + 7.99 \times 10^{-5} \frac{P(\mathbf{R})}{T(\mathbf{R})}. \quad (8)$$

The spatial statistics of the fluctuating refractive index can be expressed as a spatial power spectral density (PSD). Typically, the PSD is denoted as $\Phi_n(\kappa)$ where κ is the scalar vector wavenumber (rad/m) that describes the scalar size of the eddies in orthogonal components. It is important to note that each eddie is considered locally homogenous and spatially isotropic.

Kolmogorov theory is the most commonly used PSD model and the model used throughout this study. It is only valid for a limited regime of turbulence based on eddie size. The regime limits are called inner scale size l_0 and outer scale size L_0 . Inner scale is the size at which turbulence transitions to laminar flow while outer scale is the size at which the eddies are so large that they are no longer locally homogenous and isotropic. The expression for Kolmogorov PSD is given by:

$$\Phi_n^K(\kappa) = 0.033 C_n^2 \kappa^{-11/3} \quad \text{for} \quad \frac{1}{L_0} \ll \kappa \ll \frac{1}{l_0}. \quad (9)$$

Four other common PSD models are the von Karman, modified von Karman, Tatarskii, and Hill. These other methods are much more complex and involve different inner- and outer-scale factors that better match theory with experimental data. The dif-

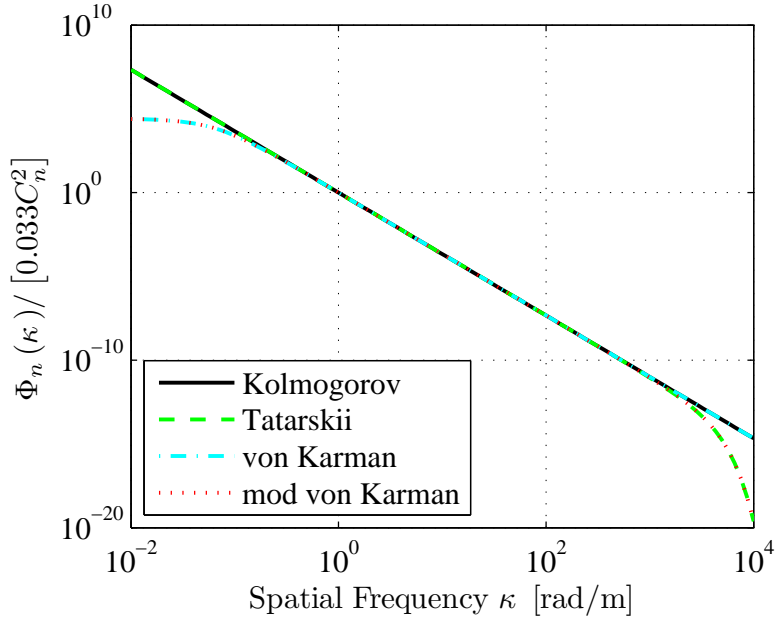


Figure 6. The comparison of different PSD models.

ferent PSD models are graphically compared in Fig 6. Even though these models are more accurate, the Kolmogorov model is easier to work with and still provides sufficient fidelity for this research.

The C_n^2 parameter in Eq. (9) is the refractive-index structure parameter measured in $\text{m}^{-2/3}$. For horizontal propagation it is often assumed to be constant, but for vertical propagation it is a function altitude h . The commonly used Hufnagel-Valley model is used for this research and is given by[13]:

$$\begin{aligned}
 C_n^2(h) = & 0.00594 \left(\frac{v}{27}\right)^2 (10^{-5}h)^{10} \exp\left(\frac{-h}{1000}\right) \\
 & + 2.7 \times 10^{-16} \exp\left(\frac{-h}{1500}\right) + A \exp\left(\frac{-h}{100}\right), \quad (10)
 \end{aligned}$$

where v is the rms wind speed and A is the nominal value at $C_n^2(0)$. Setting v to 21 m/s and A to $1.7 \times 10^{-14} \text{m}^{-2/3}$ results in the Hufnagel-Valley 5/7 model ($H-V_{5/7}$), where 5cm is the coherence diameter r_0 and $7\mu\text{rad}$ is the isoplanatic angle θ_0 . The values for r_0 and θ_0 are calculated at a wavelength of 500nm, although we adjust

these numbers for our wavelength, which is 589.2nm. Using the ($H-V_{5/7}$) model the correct r_0 and θ_0 (defined in the next subsection) are calculated along with the log amplitude variance in the following section.

2.4.2 Atmospheric Condition Characterizations.

Maxwell's equations are quantitative expressions that describe the behavior of electromagnetic waves. In the case of an atmosphere-induced, randomly-inhomogeneous, index of refraction, Maxwell's equations are solved by perturbative methods in conjunction with Green's functions. One method, Rytov theory, is typically used in conjunction with a given PSD to yield statistical moments of the field for simple sources[12][13]. Important moments include the mean value of the field and the mutual coherence function, which are then used to compute properties like the complex coherence factor, wave structure function, phase PSD, and the mean modulation transfer function (MTF). The metrics used in this research include the coherence length r_0 , the isoplanatic angle θ_0 , and the log amplitude variance σ_χ^2 , which result from Rytov theory using the Kolmogorov refractive index PSD. Some of these parameters are dependent on direction of propagation, and are manipulated for all relevant scenarios in this research. Additionally, only the analytical expressions pertaining to spherical waves for these characteristics are considered since all propagations are done with point sources.

The coherence length is a measure of the spatial coherence of light. The larger the coherence length the more coherent the light is. Figure 7 shows a simplified picture of two wavefronts and their corresponding coherence lengths. For the propagation of a point source from the ground to an altitude L directly overhead, the coherence

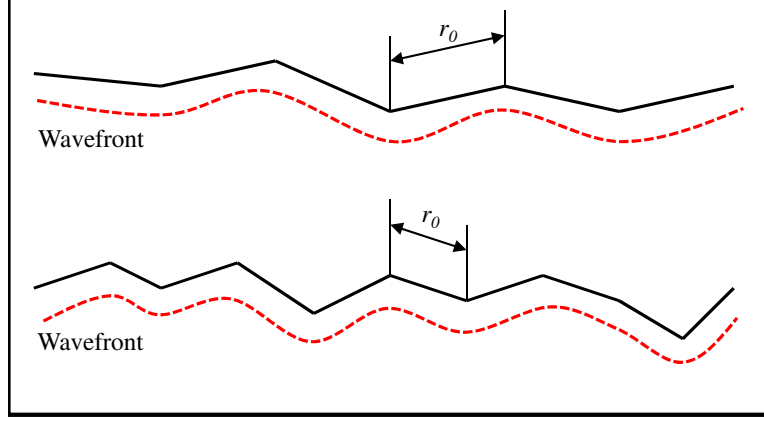


Figure 7. The coherence length estimation of two aberrated wavefronts. The top wavefront is less perturbed and, thus, has a larger r_0 . The bottom wavefront is more perturbed and has a smaller r_0 .

length is given by[13]

$$r_0^{-5/3} = 0.423k^2 \int_0^L C_n^2(h) \left(\frac{h}{L}\right)^{5/3} dh, \quad (11)$$

where k is the optical wave number. Simply substituting $h' = L - h$ into Eq. (11) gives the expression for space to ground propagation:

$$r_0^{-5/3} = 0.423k^2 \int_0^L C_n^2(h') \left(1 - \frac{h'}{L}\right)^{5/3} dh'. \quad (12)$$

The typical range is from 5cm (bad seeing) to 20cm (good seeing) for light at 500nm and vertical viewing angle.

The isoplanatic angle is a measure of how spatially-correlated the atmospheric phase distortion is for different object field angle. A large angle means that the atmosphere is well correlated for widely-separated object points. The isoplanatic

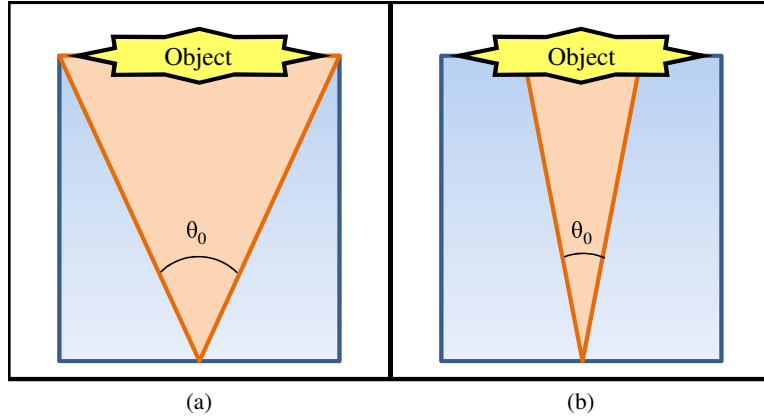


Figure 8. Two examples of the isoplanatic angle. In (a) the entire object experiences the same turbulence since it falls within θ_0 , but in (b) the object experiences uncorrelated turbulence since portions of it fall outside θ_0 .

angles for downward propagation is given by[13]

$$\theta_0^{-5/3} = 2.91k^2 \int_0^L C_n^2(h') (L - h')^{5/3} dh'. \quad (13)$$

Typical isoplanatic angles range from 5-10 μ rad for light at 500nm and vertical viewing angle. Figure 8 shows a graphic of two different isoplanatic angles. If the angle does not totally encompass the object as in Fig. 8(b) then different portions of the object lay in different turbulence realizations and experience uncorrelated turbulence effects. This makes simulating propagations much more difficult. Fortunately, all propagations take place within the same isoplanatic angle as shown in Fig. 8(a).

The log amplitude variance, also known as the Rytov number in weak turbulence, measures the amplitude fluctuations in propagated light. Typically, this is very small for vertical viewing and, for point sources, is equal for upward and downward propagations. The log amplitude variance for a spherical wave is given by[13]

$$\sigma_x^2 = 0.5631k^{7/6} \int_0^L C_n^2(h) \left(\frac{h}{L}\right)^{5/6} (L - h)^{5/6} dh. \quad (14)$$

The Rytov number for weak turbulence usually ranges from 0 (no turbulence) to 0.25. While the Rytov number has no definitive upper limit, amplitude fluctuations begin to saturate for Rytov numbers greater than 0.25 (strong turbulence).

2.5 Conventional Adaptive Optics

This section introduces the basic theory behind AO systems. It includes a breakdown of components in a typical AO system and their operation. Additionally, it discusses the system used on SOR's 3.5m telescope.

2.5.1 AO Basics.

Adaptive optics (AO) is a technology for sensing and correcting dynamic wavefront distortions in real time. The optical field of the wavefront is typically represented as a complex number in the plane transverse to propagation with amplitude A and a phase ϕ , and arranged mathematically in the form $A \exp(-j\phi)$. As light propagates through turbulence, it accumulates an additional phase ϕ_t . Mathematically, the optical field after propagation is expressed as

$$U = A \exp[-j(\phi + \phi_t)]. \quad (15)$$

Amplitude fluctuations are ignored here because they are quite small for space-to-ground propagation. Basically, the AO system senses the turbulent phase and applies its conjugate $-\phi_t$ to return the wavefront to its original form so that the compensated field is given by:

$$\begin{aligned} U &= A \exp[-j(\phi + \phi_t)] \times \exp(j\phi_t) \\ &= A \exp(-j\phi). \end{aligned} \quad (16)$$

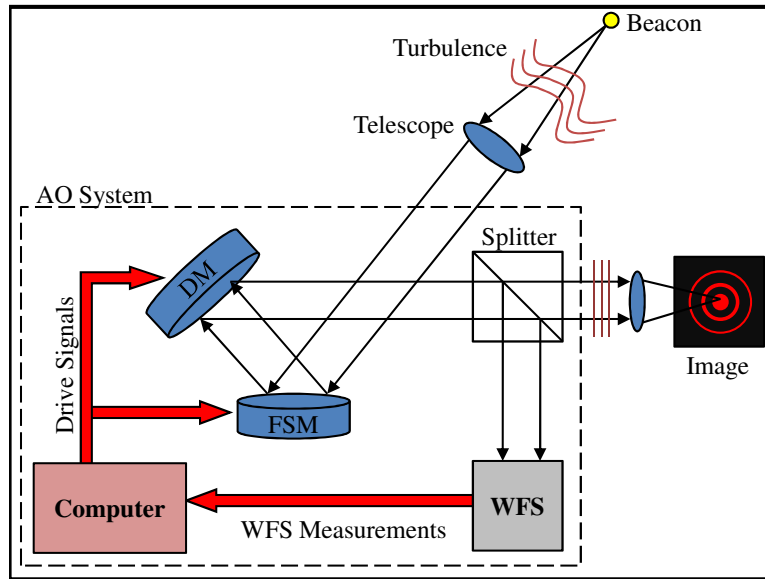


Figure 9. Basic AO system setup including the fast-steering mirror (FSM), deformable mirror (DM), and the wavefront sensor (WFS). All red components are the feedback, control loop.

Common elements in an AO system include a FSM, DM, and a wavefront sensor (WFS). These elements are connected in a feedback, control loop enabling them to communicate and compensate in real-time. Figure 9 shows a basic layout of an AO system. An incoming aberrated wavefront is captured by a telescope and collimated. The wavefront sensor detects the aberrations and commands the FSM and DM to correct for the distortions. The FSM removes the overall tilt of the wavefront and the DM corrects for all higher-order aberrations. Tilt typically comprises 87% of the overall distortion. The end result of AO compensation is typically a sharp, near diffraction-limited image of an object. The scope of this study is limited to wavefront sensor performance, using a SHWFS.

AO systems can be operated in both the closed-loop and open-loop regimes. These terms refer to the configuration of the control loop. In closed-loop, the aberrated wavefront reflects off the DM and is then sent through a beam splitter where it is captured by the WFS and a camera. The WFS detects the wavefront slopes and

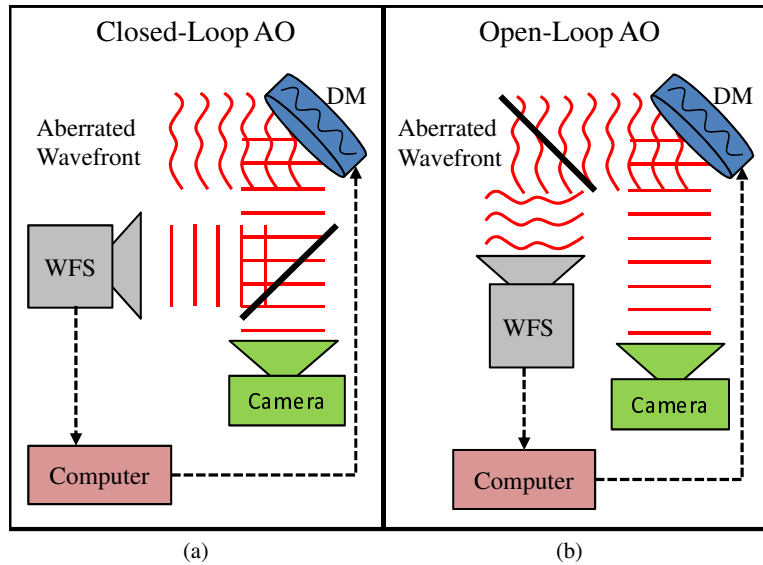


Figure 10. The two different regimes of operation for an AO system. (a) is the closed-loops regime and (b) is the open-loop regime.

commands the DM to correct the wavefront. Since the light is only sensed after it has been corrected, in this regime it is useful for measuring how well the system is compensating. In open-loop, the aberrated wavefront is detected before it has been corrected by the DM. This regime is useful for viewing the overall, evolving distortions of the wavefront. Figure 10 shows the difference between the two regimes.

2.5.2 Starfire Optical Range.

SOR is an observatory located at Kirtland AFB, New Mexico, operated by the United States Air Force Research Laboratory within its Directed Energy Directorate. They house a 3.5 meter telescope, 1.5 meter telescope, and a 1.0 meter beam director with AO technology designed for satellite tracking. This requires very high frame rates and a fast slewing gimbal which is uncommon amongst most modern observatories. Considered forerunners in AO, SOR was the first site to demonstrate an operational closed-loop AO system utilizing an LGS[6][14]. Their primary mission is to develop and demonstrate optical wavefront control technologies, and support field experiments



Figure 11. The 3.5 meter telescope at SOR. This long exposure photo shows the exposed telescope aperture and the sodium LGS.

by others within the research community. Figure 11 shows a picture of the main telescope.

The AO components used by SOR are briefly discussed here. The 3.5 meter Cassegrain telescope is contained within a retractable dome which allows the aperture to be completely exposed as shown in Fig. 11. This enables the telescope to follow fast-slewing objects by drastically reducing the weight on the gears. The telescope's exit pupil is imaged onto a 21cm DM containing 30 actuators per side. A SHWFS is used with a lenslet array in the conjugate pupil plane to sense the incident wavefront[15]. The beacon for the AO system is artificially created by a sodium LGS which can also be seen Fig. 11. Figure 12 shows an image of the k-Peg binary stars before and after compensation. This image was captured in 1997 and constituted the first light for the AO system[14]. It should be noted that the images are auto-scaled, so the increased peak intensity in the compensated image is not evident.

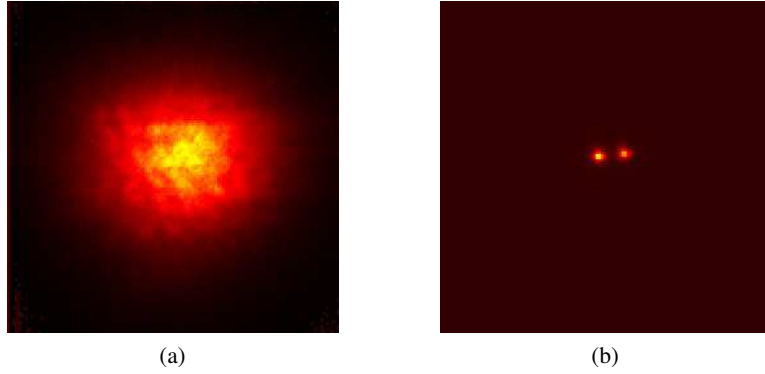


Figure 12. The binary star system known as k-Peg as seen by SOR’s 3.5 meter telescope, uncompensated image (left) and compensated image (right). These images are auto-scaled, hiding the increased peak intensity in the compensation image.

2.6 Shack-Hartmann Wavefront Sensor

This section explores the SHWFS in AO systems. First, the historical development of the WFS is discussed. Next, principles of operation are explored. Finally, perspective elongation error is introduced.

2.6.1 History and Development.

The SHWFS is the and most common WFS used in AO. The SHWFS is an improvement on the Hartmann Screen Test developed by Johannes Hartmann in the early 1900s. His simple and effective methodology involved placing a hole-filled screen over the aperture of the telescope and studying exposed photographic plates placed on either side of the focal point in image space. The screen caused light to pass through different entrance pupil locations and show up as a “spot diagram on each plate. By comparing the corresponding spot locations on the plates, he could determine where aberrations resided on the lens[16].

After nearly 70 years with little improvement on the Hartmann Screen, the United States Air Force (USAF) became interested in improving images of satellites taken from Earth in the 1960s. They assigned the task to the Optical Science Center (OSC)

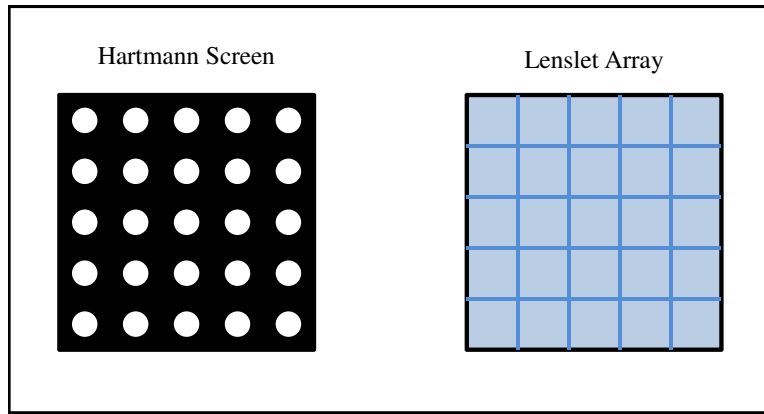


Figure 13. The Hartmann screen (left) and the lenslet array (right). The lenslet array uses all incident photons while the Hartmann screen only uses photons incident on each hole.

at the University of Arizona. Dr. Aden Mienel and Dr. Roland Shack, researchers there, applied the Hartmann Screen Test to sensing atmospheric distortions[17].

Due to very low intensity of light from observed objects in space, Dr. Shack replaced the holes in the screen with lenses to focus the light. He then optimized photon use by placing lenses directly beside each other in an array pattern; a design that ensured that no photon was wasted by hitting the space between the lenses. Finally, he moved the lens array from the aperture to in front of the eyepiece. By placing a beam splitter between the eyepiece and a collimating lens, the main beam continued to the camera while the other was passed to the array of lenses[17]. Figure 13 shows an example of the original Hartmann screen and the modern SHWFS lenslet array.

2.6.2 Principles of Operation.

The beauty of the SHWFS lies in its simple yet effective way of measuring wavefront slopes. The lenslets, mentioned in the previous section, are affixed in front of a detector array as shown in Fig. 14. In order to obtain small focal spots close to the diffraction limit, the lenslets are typically sized so that, when imaged onto the

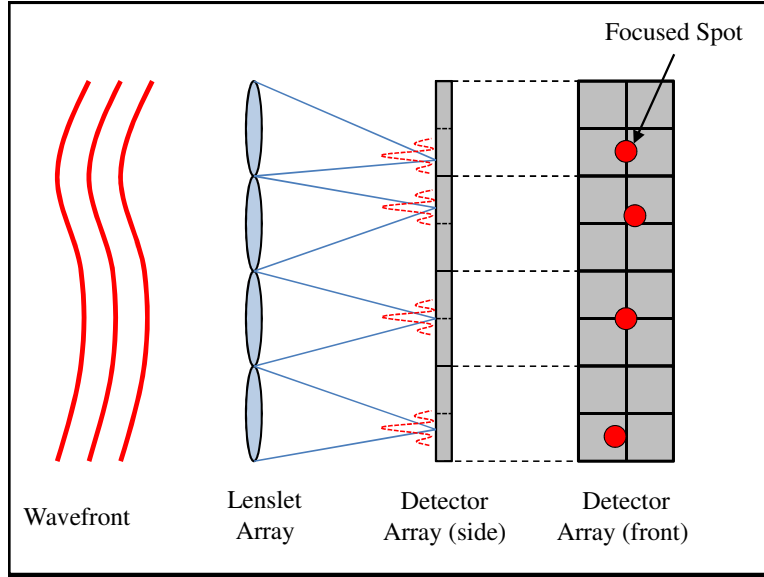


Figure 14. Basic setup of a Shack-Hartmann wavefront sensor. Each lenslet focuses a localized piece of the wavefront to a detector to calculate the slope.

primary mirror, they are roughly the size of the coherence length r_0 . Additionally, each lenslet corresponds to a distinct region of pixels on the detector. When light is incident on the lenslet array, the local field is focused onto its corresponding area of detector pixels[18].

In order to calculate wavefront slopes effectively, the detector array must be able to detect the centroids of the focused spots. Two methods are commonly used: quad cell detection and centroid estimation of light intensity. A close up of a quad-cell sensor from Fig. 14 is shown in Fig. 15. Each quadrant is the size of a pixel, with the sensor centered at the origin of the $x - y$ plane. The position of the focused beam (T_x and T_y) can be determined by comparing the intensity of light incident on the positive and negative halves of each axis as follows:

$$T_x = \frac{(C + D) - (A + B)}{A + B + C + D} \quad (17)$$

$$T_y = \frac{(A + D) - (B + C)}{A + B + C + D}. \quad (18)$$

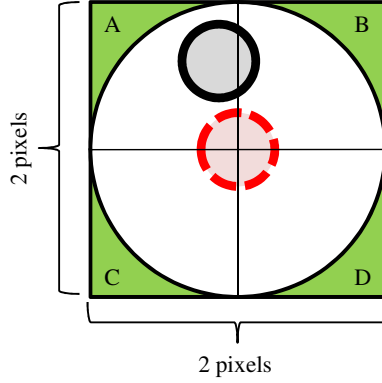


Figure 15. An example of a quad-cell detector.

In the above equation, A , B , C , and D represent the intensity of light incident in each quadrant.

The other method, centroid estimation, is performed by computing the normalized, first moment of the irradiance pattern. Like the previous method, the origin is defined at the center of the subaperture and the $x - y$ coordinates of the focused light are calculated by:

$$T_x = \frac{\int_A \int x I(x, y) dx dy}{\int_A \int I(x, y) dx dy} \quad (19)$$

$$T_y = \frac{\int_A \int y I(x, y) dx dy}{\int_A \int I(x, y) dx dy}, \quad (20)$$

where A is the area of the subaperture and $I(x, y)$ is the irradiance of the focused spot.

Once the position of the focused spot has been determined, simple geometry is applied to determine the wavefront slope as shown in Fig. 16. In general, tilt sensing is a two-dimensional problem, but without loss of generality, we can treat the tilt as a one-dimensional problem[18]. The slope of the tilted wavefront with respect to the reference wavefront can be represented by dW/dy . Using similar triangles as shown

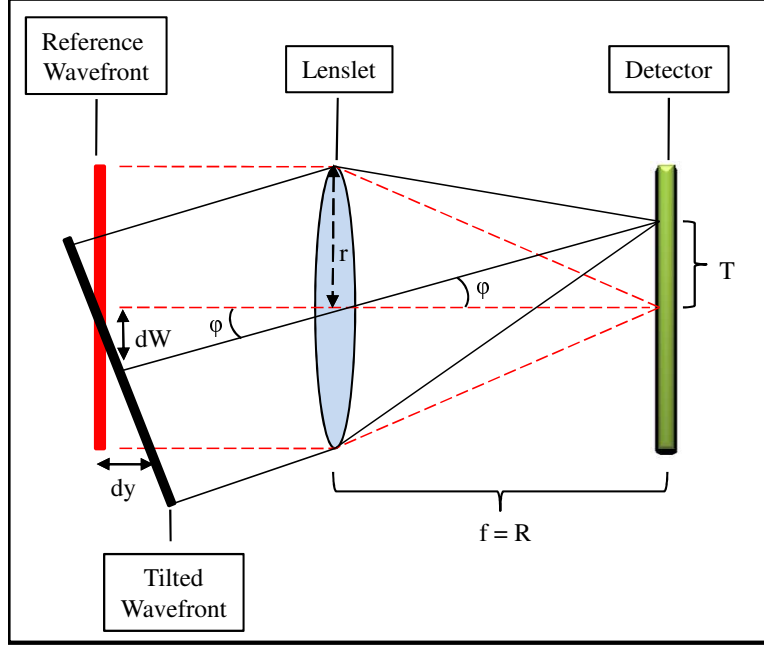


Figure 16. Geometry of a localized portion of a wavefront incident on a lenslet and focused on a detector.

in Fig. 16, we can determine that

$$\frac{dW}{dy} = -\frac{T}{R}, \quad (21)$$

where T is the centroid location and R is the radius of curvature. Introducing normalized pupil coordinates $\rho = y/r$ to Eq. (21) yields:

$$\frac{dW}{dy} = \frac{dW}{d\rho} \frac{d\rho}{dy}, \quad (22)$$

where $d\rho/dy$ is easily calculated as $1/r$. Substituting Eq. (22) into Eq. (21) and rearranging gives an expression for localized tilt:

$$\frac{dW}{d\rho} = -\frac{rT}{R}. \quad (23)$$

Calculating this for every lenslet and stitching together each localized portion of

the wavefront effectively reconstructs the original wavefront incident on the Shack-Hartmann sensor.

2.6.3 Perspective Elongation.

While several errors and noise sources exist within the SHWFS, we are only concerned with one source of error: spot elongation. When an ideal point source is used as a beacon for the AO system in vacuum, the light is focused down to perfect, circular spots in SHWFS subapertures. However, the spots can become elongated due to diffraction, atmospheric effects, imperfect laser quality, and beacon scattering depth[2]. These elongated spots lead to errors in centroid calculations, which in turn lead to incorrect slope measurements[6]. LGS's are used to create beacons in the sky and are typically launched from the side of the telescope. The amount of elongation is proportional to the separation between the LGS launching system and the telescope[3]. SHWFS spots are elongated differently based on each subaperture's viewing angle relative to the beacon scattering spot, with the subapertures furthest from the laser showing the most elongation error[6, 5]. This phenomenon is typically referred to as perspective elongation. Figure 17 shows a simulation of perspective elongation[4].

2.7 Gaussian Beams

Like many lasers, LGS beacons can be modeled as a Gaussian beam which have several desirable mathematical properties. Gaussian beams remain Gaussian after propagation through vacuum, although their beam radius and wavefront radius of curvature evolve. Also, beam properties in the receiver plane can be easily calculated from beam properties in the source plane or vice-versa. A Gaussian field in the source

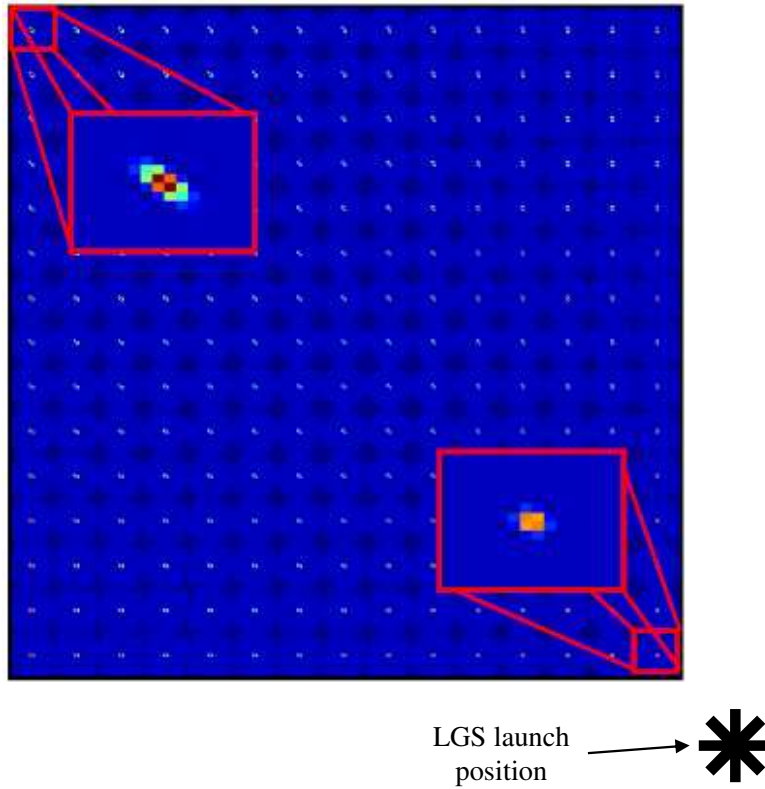


Figure 17. An example of perspective elongation. In this case, the LGS beacon is launched from the bottom right corner which causes the greatest elongation in SHWFS spots in the top left corner[4].

plane is given by[12]:

$$U(x, y, 0)_{\text{gaus}} = \exp\left(-\frac{r^2}{W_0^2}\right) \exp\left(j\frac{kr}{2F_0}\right) \quad (24)$$

where W_0 is the source beam radius and F_0 is the source radius of curvature.

For any propagation distance z normal to the $x - y$ plane, the Gaussian field and intensity are given by[12]:

$$U(x, y, z)_{\text{gaus}} = \frac{1}{\Theta_0 + j\Lambda_0} \exp\left(-\frac{r^2}{W^2}\right) \exp\left(-j\frac{kr^2}{2F}\right) \quad (25)$$

$$I(x, y, z)_{\text{gaus}} = \frac{1}{\Theta_0^2 + \Lambda_0^2} \exp\left(-\frac{2r^2}{W^2}\right), \quad (26)$$

where Θ_0 is the amplitude change due to focusing, Λ_0 is the amplitude change due to diffraction, W is the beam radius at z , and F is the radius of curvature at z . As stated above, these beam parameters can be calculated from source parameters as follows:

$$\Theta_0(z) = 1 - \frac{z}{F_0} \quad (27)$$

$$\Lambda_0(z) = \frac{2z}{kW_0^2} \quad (28)$$

$$W(z) = W_0 \sqrt{\Theta_0^2 + \Lambda_0^2} \quad (29)$$

$$F(z) = \frac{F_0 (\Theta_0^2 + \Lambda_0^2) (\Theta_0 - 1)}{\Theta_0^2 + \Lambda_0^2 - \Theta_0}. \quad (30)$$

While the above theory applies to Gaussian beam propagation in vacuum, an expression for the mean turbulence-degraded irradiance of an initially Gaussian beam has been developed. Closed-form expressions for Gaussian beams through turbulence are involved to derive, but one common expression is mean intensity at any given

propagation distance given by[12]:

$$\langle I(\mathbf{r}, z) \rangle = \frac{W_0^2}{W^2} \exp\left(-\frac{2r^2}{W^2}\right) \exp[2\sigma_r^2(\mathbf{r}, z) - T], \quad (31)$$

where σ_r^2 describes the atmospherically induced change the transverse direction, and T describes the change in the on-axis mean irradiance at the receiver plane caused by turbulence. Both terms are proportional to the reverse-path r_0 value from Eq.(12) as evident in the expressions:

$$\sigma_r^2(\mathbf{r}, z) = 3.62k^{7/6}z^{5/6}\Lambda^{5/6}\frac{r^2}{W^2}\int_0^L C_n^2(h)\left(1-\frac{h}{L}\right)^{5/3}dh \quad (32)$$

$$T = 4.35k^{7/6}z^{5/6}\Lambda^{5/6}\int_0^L C_n^2(h)\left(1-\frac{h}{L}\right)^{5/3}dh \quad (33)$$

With a minor rearrangement of Eq. (12), Eqs. (32) and (33) can be rewritten in closed form as:

$$\sigma_r^2(\mathbf{r}, z) = 8.30\frac{r^2}{W^2}\left(\frac{\Lambda L}{kr_0^2}\right)^{5/6} \quad (34)$$

$$T = 9.98\left(\frac{\Lambda L}{kr_0^2}\right)^{5/6}. \quad (35)$$

It should be noted that Eq. (31) is the ensemble average irradiance (also called long-exposure) that assumes the beam is not tracked.

2.8 Laser Guide Stars and Sodium Layer Properties

As shown in Fig. 9, the AO system requires a light source or beacon to gather wavefront data. And, as mentioned in the introduction, observatories like SOR, Keck, and others have begun relying on sodium LGS's as a wavefront reference source[3, 4].

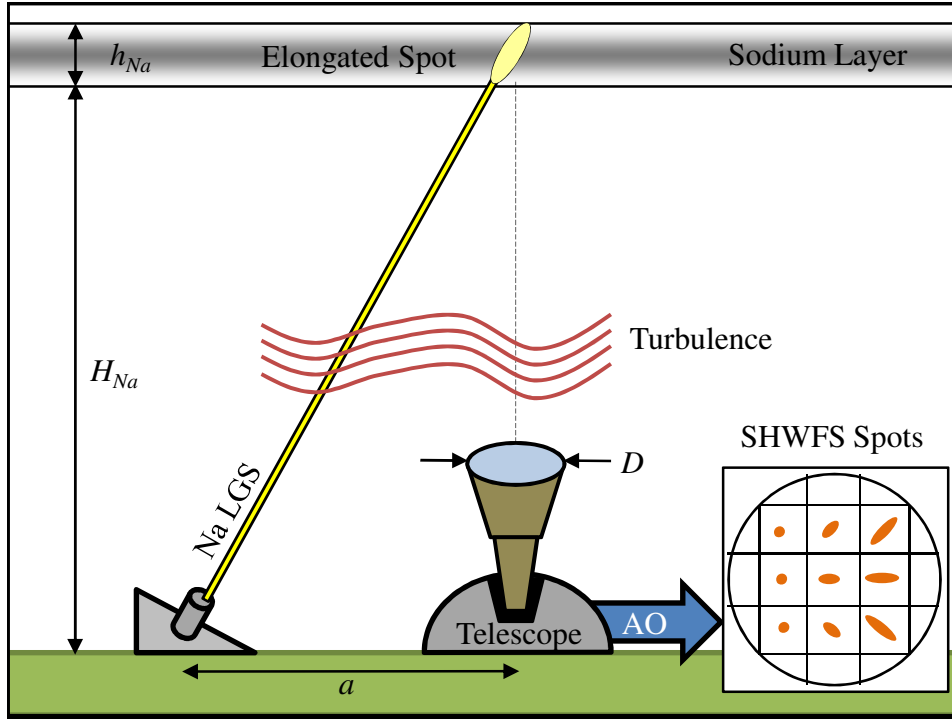


Figure 18. An elongated beacon caused by the depth h_{Na} of the sodium layer results in elongated spots in SHWFS subapertures.

Figure 11 shows the beam of the sodium LGS launched at the SOR. At a wavelength of 589.2nm and separated a distance a from the center of a telescope aperture D , sodium LGS's excite atoms in the mesosphere as shown in Fig. 18.

Using the sodium layer to create artificial beacons has several advantages and disadvantages. To fully understand them, sodium layer properties are described here. The mesosphere contains a buildup of neutral sodium atoms located at a mean height H_{Na} of 90km. The depth of the sodium layer h_{Na} can vary from 5-20km depending on location, season, and even time of day[19, 20]. While the origins of sodium atom buildup in the mesosphere is unknown, it has been hypothesized that it was formed from the ablation of meteors[21]. Studies have shown that the distribution of sodium atoms is Gaussian as shown in Fig. 19[6, 21]. At different distances H_L from the the

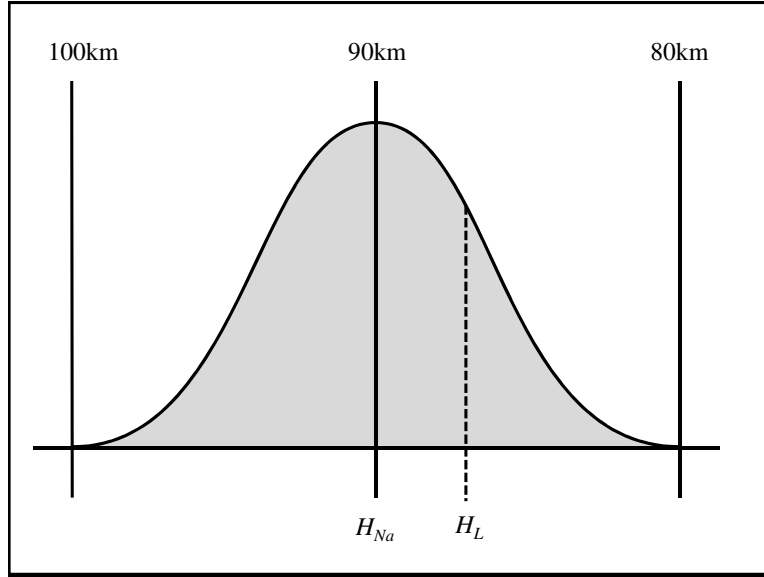


Figure 19. Model column density of sodium atoms in the mesosphere at a mean height H_{Na} of 90km.

mean, the column density can be approximated by

$$f(H_L) = \exp\left[-\frac{(H_{Na} - H_L)^2}{W_L^2}\right], \quad (36)$$

where W_L from the full-width, half-max as $5\text{km}/\sqrt{\ln 2}$.

When the sodium atoms are excited by the laser, they emit light becoming a beacon for the AO system. These beacons can be placed anywhere in the sodium layer, theoretically enabling the system to image anything in the sky, including fast-moving objects. Additionally, the beacons are brighter than natural stars which gives the AO system an ample amount of photons to work with. The problem comes with the depth of the sodium layer. As mentioned before, an ideal beacon is a point source, but the depth forms an oblong three-dimensional scattering volume when excited by the laser leading to one of the causes of perspective elongation discussed in Sec. 2.6.

2.9 Imagery Comparison Techniques

Perspective elongation is simulated multiple times using different methods of modeling an elongated beacon in the sodium layer. To determine the optimal elongated beacon model, it was necessary to compare the elongated spot images in SHWFS sub-apertures. The two methods chosen in this research were root mean squared (RMS) error and correlation. The following subsections explain both methods in more detail.

2.9.1 Root Mean Square Error.

The RMS error is typically used to measure the differences between simulated values from a model and actual values from the thing being modeled. This method determines the model's precision. The mathematical definition is given by

$$RMS_{diff} = \sqrt{\langle (\gamma_{n+1} - \gamma_n)^2 \rangle}, \quad (37)$$

where γ_n is an arbitrary symbol for a data set or value and $\langle \dots \rangle$ is the ensemble average. A slight variation on the RMS error is the RMS percent difference. This method is essential the same as the RMS error calculation except it gives the percent difference. The mathematical definition is

$$RMS_{\%diff} = \sqrt{\left\langle \left(\frac{\gamma_{n+1} - \gamma_n}{\gamma_n} \right)^2 \right\rangle}. \quad (38)$$

2.9.2 Correlation.

Another useful comparison technique is called correlation. Correlation is a statistic measuring the dependence between two or more data sets. One way to measure correlation is by calculating the correlation coefficient ρ . This is a number that ranges from from -1 to 1 where -1 is completely anticorrelated, 0 is completely uncorrelated,

and 1 is completely correlated. Values close to -1 or 1 are considered highly correlated and thus very dependant, while values close to 0 are considered highly uncorrelated and thus independent. The mathematical expression for the correlation coefficient is given by:

$$\rho_{A,B} = \text{corr}(A, B) = \frac{\text{cov}(A, B)}{\sigma_A \sigma_B} = \frac{\langle AB \rangle - \langle A \rangle \langle B \rangle}{\sigma_A \sigma_B}, \quad (39)$$

where A and B are data sets, $\langle \dots \rangle$ is the ensemble average, and σ is the standard deviation. Since the definition manipulates different statistical moments, it is very useful for comparing images formed by the data instead of the raw values of the data themselves.

2.10 Chapter Summary

In summary, AO systems use beacons to collect data on distorted wavefronts. The distortions are caused by inherent turbulence in Earth's atmosphere. Although ideal beacons, natural stars of the required brightness are rare, so Gaussian lasers are used to create artificial beacons in the sodium layer of the atmosphere. This enables optical systems, like the observatory at SOR, to image almost anything in the sky. Unfortunately, the artificial beacons are distorted due to the depth of the sodium layer and the separation from the telescope aperture. A distorted beacon causes non-uniform spots in SHWFS subapertures. This leads to an inaccuracy of wavefront slope measurements and a lost in the image resolution of the optical system. Chapter III discusses methods used to accurately simulate the distorted beacon and form elongated spots in SHWFS subapertures.

III. Research Methodology

This chapter explains describes the methodology for both simulations and experiments used in this research. The goal of this research was to develop models that accurately simulated perspective elongation in SHWFS subapertures, and was done in two parts. The first part used MATLAB to model the elongation by testing a method described in current literature. The simulation was used to determine how accurate the documented method was. The second part used a special source in an optics laboratory to recreate the elongation in a real SHWFS. The experimental result was then compared to the MATLAB simulation for validation.

3.1 Computer Simulation Environment

To study perspective elongation in SHWFS subapertures, it was necessary to simulate an elongated beacon in the sodium layer. This was done by simulating the propagation of a Gaussian beam through the atmosphere, from ground to sky. Controlling how the beam interacted with the sodium layer created the elongated beacon. Once the beacon was manipulated to resemble the beacon shape observed at SOR, it was propagated back through the atmosphere and the SHWFS. For simplicity, a telescope was omitted in all simulations and the SHWFS lenslet array was placed at the primary aperture plane instead. The telescope was not necessary since it only demagnifies the image and has no direct effect on perspective elongation. Additionally, all simulations were done in open-loop as described in Sec. 2.5 to show the evolution of the elongated spots. Figure 20 shows a basic layout of the simulation geometry including the parameters. It should be noted that a 2m aperture separated 4m from the LGS launching system was used instead of the SOR specifications of a 3.5m aperture separated 2.5m from the LGS launching system. Since the total

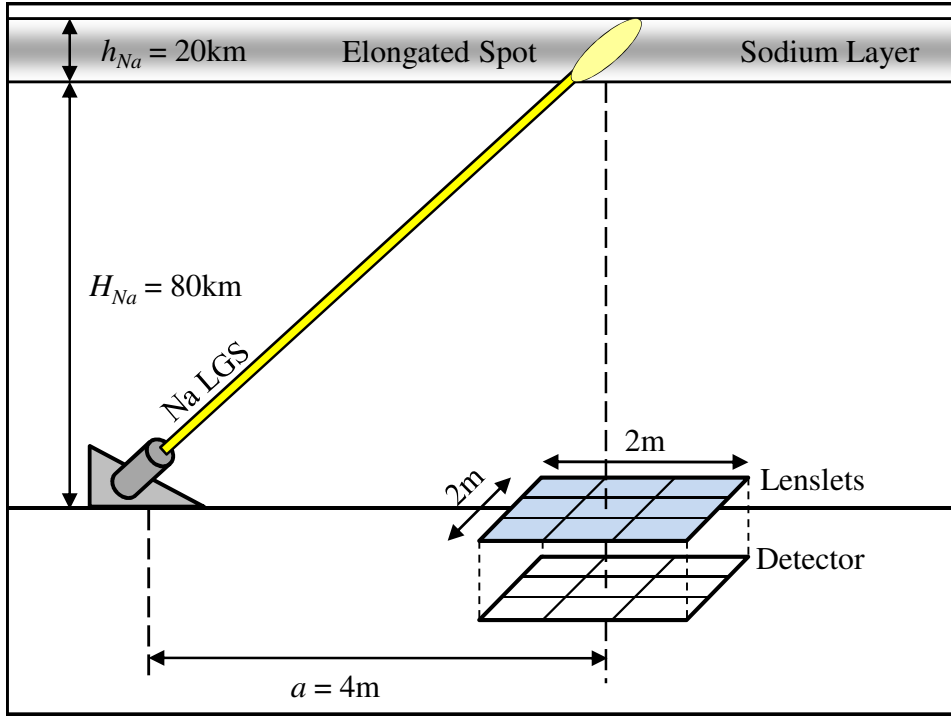


Figure 20. The basic setup of the software model geometry. The telescope is replaced with SHWFS lenslets to simplify the setup.

distance for both scenarios is the same (6m), our setup basically recreates the same geometry used at SOR. The smaller aperture greatly reduced simulation times while keeping the subaperture geometry the same.

Elongated beacons in the sodium layer are difficult to simulate because they are three-dimensional scattering volumes. Research shows that they can be simulated by dividing the sodium layer into multiple, evenly-spaced slices and propagating a Gaussian beam from a fixed location on the ground to each slice[5]. This creates a different intensity pattern in each individual slice. In past studies seven slices in the sodium layer were used without verification to create these scattering volumes[5]. Figure 21 shows the division of the sodium layer into seven slices.

While using seven slices does form the elongated beacon and recreates the perspective elongation in SHWFS subapertures, the accuracy of this configuration has not been reported. To test this method, the elongated beacon was modeled 19 times,

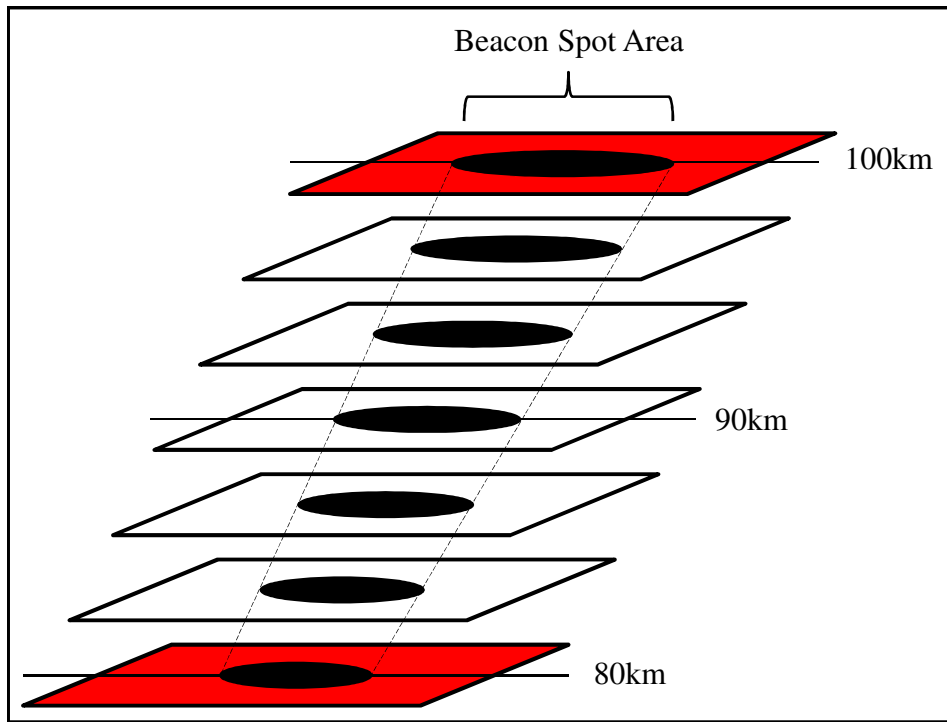


Figure 21. The sodium layer divided into discrete slices between 80km and 100km.

each time using an increasing, odd number of evenly-spaced sodium layer slices from 3 to 39. Each elongated beacon was then imaged by a SHWFS, resulting in elongated subaperture images. Comparing the elongated spots revealed the minimum number of sodium layer slices needed.

To insure the perspective elongation was recreated properly, several pieces were individually simulated and verified. Since the WaveProp software was used for nearly all facets of software simulation, typical verification entailed performing the desired propagation/modeling in WaveProp and comparing the results to theory. The following subsections provide the verification of the following parameters: grid sampling, atmospheric turbulence characteristics, and Gaussian beam propagation.

Table 1. Sampling parameters for all wave propagations.

Parameters	Upward	Downward
Grid size N	1024	1024
Grid spacing (source) δ_1 [mm]	4	4
Grid spacing (observation) δ_n [mm]	10	10
Max propagation distance Δz_{max} [km]	27.8	27.8
Number of propagations n	10	10

3.1.1 Grid Sampling.

To properly simulate the propagation of light on a finite grid, the sampling parameters were carefully determined from the method outlined in Sec. 2.3. For the propagation of the Gaussian beam from ground-to-sky, the source diameter D_1 was set to 8cm, the diameter of the object in the observation plane D_n was set to 1.25m, and the propagation distance z was set to 90km. These lengths were similar to actual specifications of the LGS AO system used at SOR. To satisfy all four sampling inequalities, they were plotted on the same chart and analyzed. As shown in Fig. 22 the contour lines represent different grid sizes N and the dashed line represents constraint 1. Constraints 2 and 3 are not shown because they plotted well out of the range and essentially do not impact the sampling analysis. The sampling parameters from ground-to-sky are more stringent than those from sky-to-ground, so the same parameters were used for all propagations. Table 1 lists the parameters used in the simulations.

3.1.2 Atmospheric Characteristics and Verification.

To accurately simulate perspective elongation, an atmospheric model was developed. As outlined in Sec. 2.4, the atmosphere can be defined with quantitative parameters such as the coherence length r_0 , isoplanatic angle θ_0 , and the Rytov number σ_χ^2 . Using the equations in Sec. 2.4 the atmospheric parameters for this study are

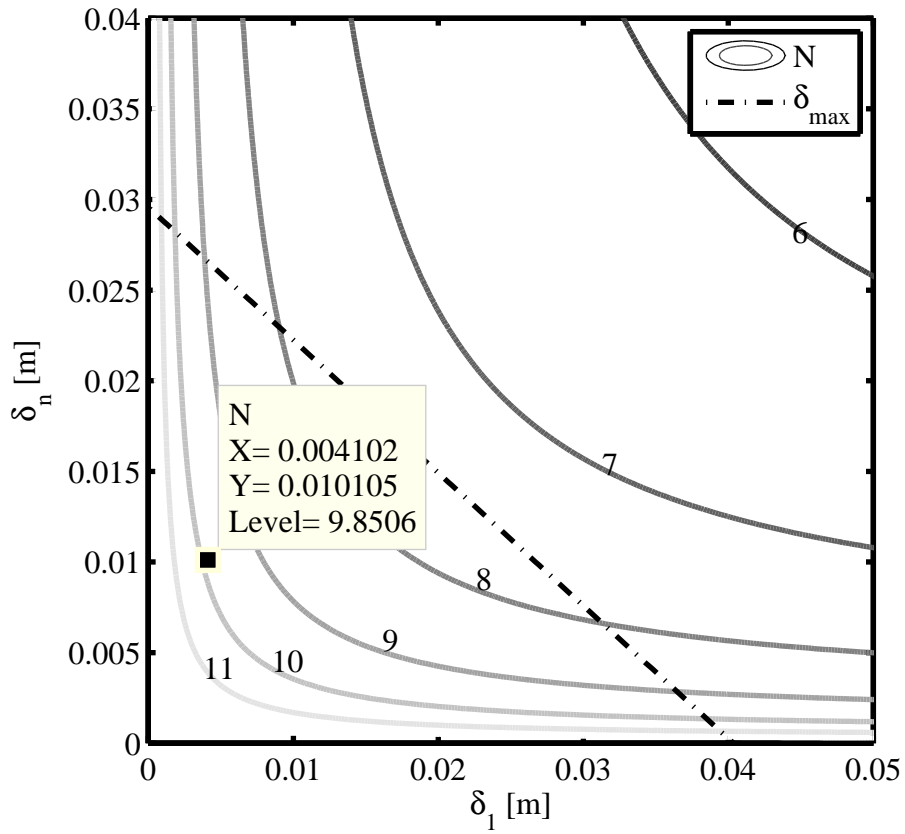


Figure 22. A plot of the sampling inequalities. The contour lines are different grid sizes N and the dashed line is the maximum boundary for the grid spacing parameters δ_1 and δ_n . The data point shows the chosen parameters.

Table 2. Theoretical atmospheric parameters for vertical upward and downward propagation paths.

Metric	upward	downward	
r_0 [m]	2.40	0.0619	n n
θ_0 [μ rad]	—	8.402	
σ_χ^2	0.045	0.045	

shown in Table 2 for both the ground-to-sky (upward) and sky-to-ground (downward) propagations. All characteristics were calculated were point sources. A wavelength of 589.2nm and a propagation distance $L = 90\text{km}$ was used in all calculations. As evident in the table, the parameters fall within their expected ranges. Since all values were calculated for vertical propagation paths, the overall turbulence is relatively weak, with a Rytov number of only 0.045.

The atmospheric parameters were then used to program a three-dimensional turbulence model in WaveProp. A three-dimensional model more accurately simulates the effects of turbulence and, in this case, consisted of 10 phase screens placed along the propagation path. To verify that the model accurately simulated Kolmogorov turbulence, the coherence length was tested for a single phase screen. Finally, tests to verify the coherence length and Rytov number for the entire three-dimensional model were performed.

To verify r_0 for a single phase screen, the phase structure function D_ϕ was computed and compared to theory. For the Kolmogorov spectrum, the phase structure function is given by[10]:

$$D_\phi(\Delta r) = 6.88 \left(\frac{\Delta r}{r_0} \right)^{5/3}, \quad (40)$$

where Δr is the spatial separation between points. Using the coherence length r_0 for downward propagation in Table 2, phase screens, such as the one shown shown in Fig. 23, were generated in WaveProp. Because of the random nature of phase screen generation, 100 phase screens and their corresponding phase structure functions were

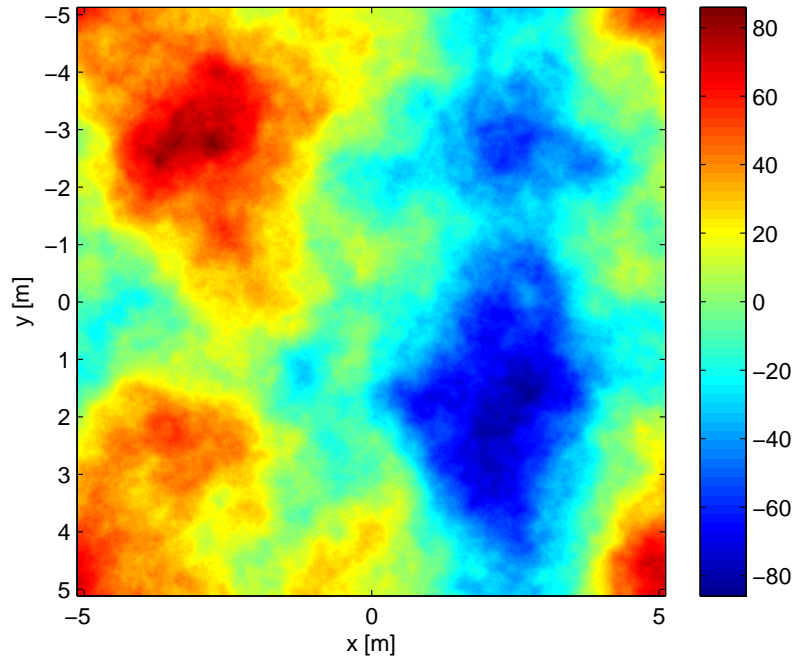


Figure 23. A randomly-generated Kolmogorov phase screen.

computed and averaged. Figure 24 shows a plot of the theoretical and simulated $D_\phi(\Delta r)$. As evident in the figure, the functions match up as well as the simulation method allows.

Similarly to the single phase screen, the 3D turbulence model was verified with the same phase structure function $D_\phi(\Delta r)$ in Eq. (40). Using the same r_0 value, 100 phase structure functions were simulated and averaged in MATLAB. Figure 25 shows a plot of the theoretical and simulated $D_\phi(\Delta r)$. The functions match up well, thus verifying that the turbulence model is behaving as anticipated.

To verify the σ_χ^2 , the log-amplitude PDF was calculated first. An on-axis point source located at a height of 90km from the aperture plane was propagated through a single Kolmogorov phase screen and vacuum. The on-axis log amplitude χ was then calculated by [8, 12]:

$$\chi = \ln \left(\frac{|U_t|}{|U_0|} \right), \quad (41)$$

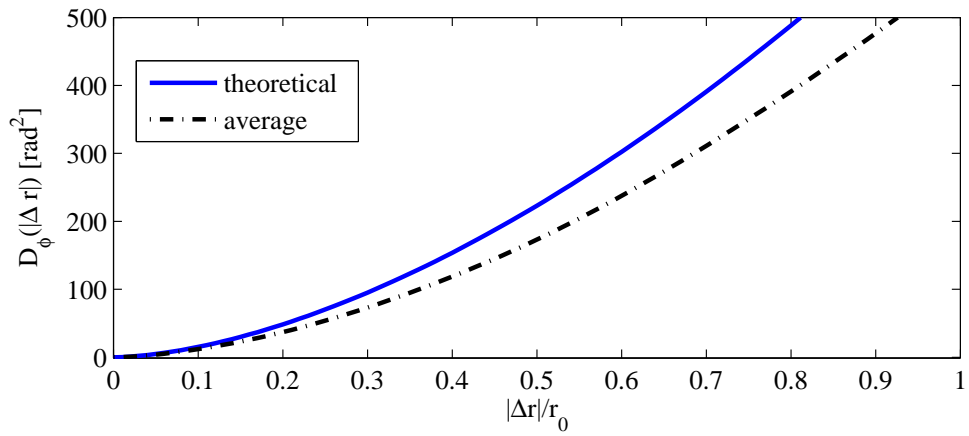


Figure 24. The theoretical (blue) and the simulated (black) structure functions for a single Kolmogorov phase screen. The simulated structure function was found by averaging 100 randomly generated structure functions.

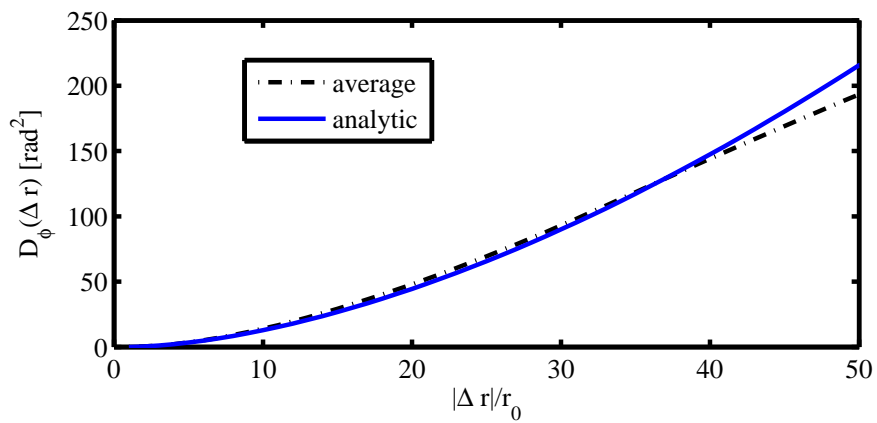


Figure 25. The theoretical (blue) and the simulated (black) structure functions for the three-dimensional (10 screen) Kolmogorov turbulence model. The simulated structure function was found by averaging 100 randomly generated structure functions.

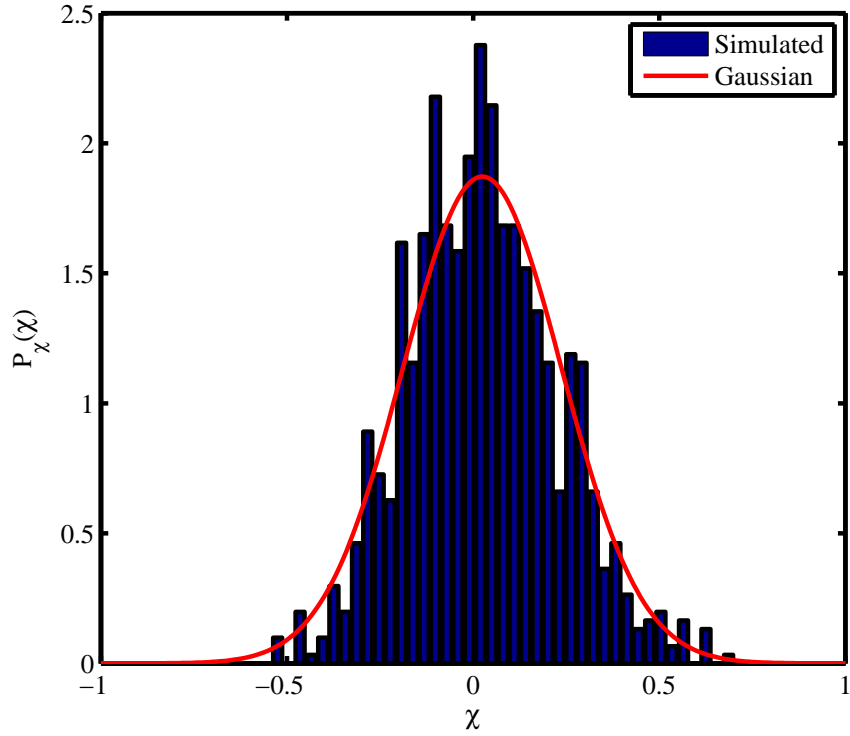


Figure 26. Comparison of the on-axis log amplitude with a Gaussian PDF.

where $|U_t|$ is the amplitude of the field through turbulence and $|U_0|$ is the amplitude of the field through vacuum. Due to the random nature of the turbulence model, 1000 realizations of the propagation were executed, and the log amplitude was calculated for each. Only the on-axis grid points were used in each calculation. Results were plotted in a histogram and compared to a Gaussian PDF as shown in Fig. 26. To further verify the Rytov number, the RMS error was tested for several Rytov numbers between 0 and 0.1 using the results from the histogram. Figure 27 shows a plot of the RMS error. The resultant Rytov number is close to the theoretical value in Table 2. With a valid turbulence model, propagations of light through the atmosphere will behave as expected and can be verified with theory as discussed in the next subsection.

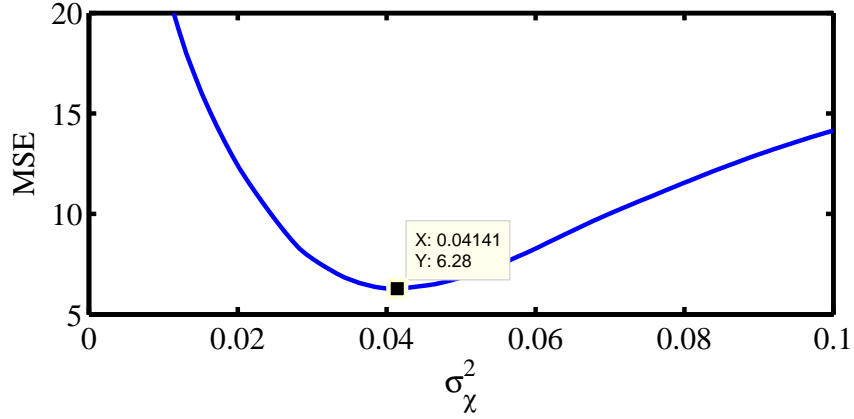


Figure 27. The mean squared error plot to locate the simulated Rytov value.

3.1.3 LGS Beam System Parameters.

The laser used in the LGS system was modeled as a Gaussian beam. Using the specification from SOR, the source diameter W_0 was set to 8cm and the source radius of curvature F_0 was set to 90km [19, 20]. These variables were kept constant when calculating the source amplitude parameters due to focus Θ_0 and diffraction Λ_0 for different propagation distances z . The beam parameters W and F in the observation plane were then calculated from the source parameters. Propagation distances were set by the number of slices used to divide the sodium layer. Table 3 shows data for all parameters used in the 7 slice scenario. It should be noted that the Gaussian laser was not focused to the mean of the sodium layer (90km). Figure 28 shows the spot size trend for vacuum propagation of the beam from ground to sky. The graph shows that the beam focuses around 10km, well before the mean of the sodium layer. However, the beam waist only increases approximately 5cm over the entire depth of the sodium layer (20km). The code used to model Gaussian beam parameters is shown in Listing A.1 of Appendix A.

The source beam parameters were then programmed into WaveProp and propagated to various slices (distance) in the sodium layer. This effectively formed the

Table 3. Theoretical data for Gaussian beam vacuum propagation from ground to sky. This is for the scenario of dividing the sodium layer into 7 slices.

	propagation distance z [km]						
	80	83.333	86.667	90	93.333	96.667	100
W_0 [cm]	8	8	8	8	8	8	8
F_0 [km]	90	90	90	90	90	90	90
Λ_0	2.4909	2.5397	2.5886	2.6374	2.6862	2.7351	2.7839
Θ_0	0.0556	0.037	0.0185	0	-0.0185	-0.037	-0.0556
W [cm]	19.93	20.32	20.71	21.10	21.49	21.88	22.28
F [km]	-85.768	-87.176	-88.578	-90	-91.432	-92.874	-94.324

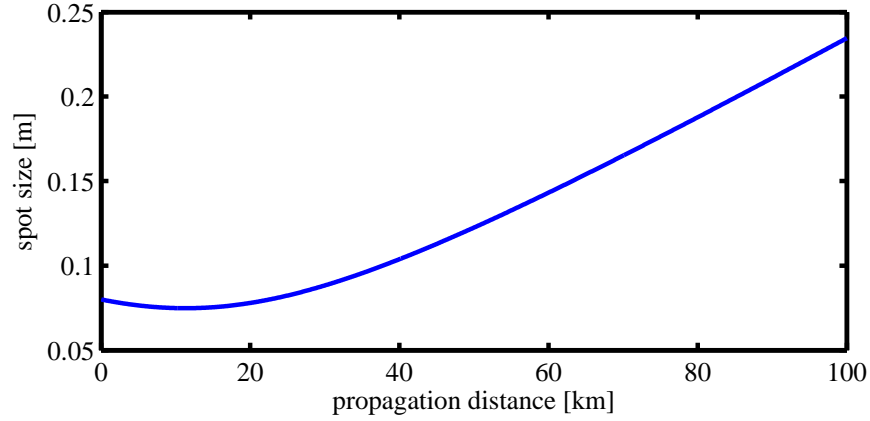


Figure 28. A graph showing the trend of the spot size from ground to the outer edge of the sodium layer (100km). The waist forms around 10km, but the beam size increases very slowly through the entire propagation.

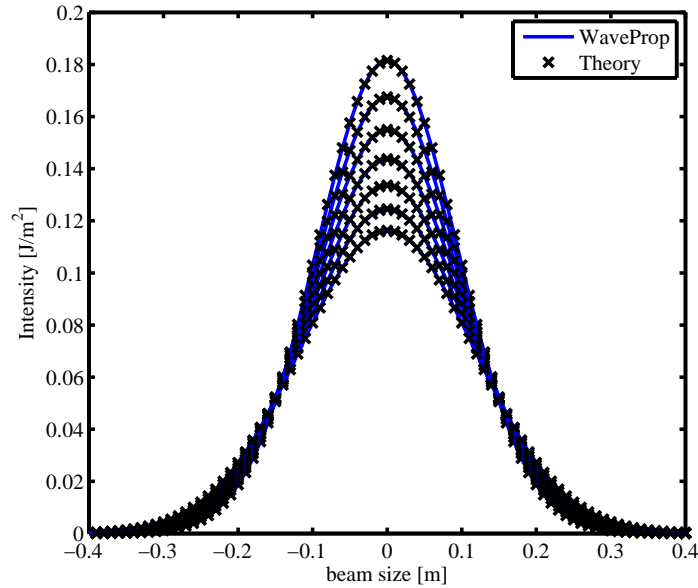


Figure 29. The center cutaway of the Gaussian beam vacuum propagation to 7 slices of the sodium layer. The simulation result (blue) match perfectly with the theoretical expressions (black).

elongated beacon model. To verify the beams propagated correctly, the $y = 0$ cutaway of the intensity pattern at each slice was compared to theory. This was done in vacuum propagation for the 7 slice scenario and shown in Fig 29. As evident in the figure, the models match perfectly with the theoretical expressions. Listing A.2 in Appendix A shows the code used to propagate and verify Gaussian beams.

For the turbulence scenario, the beams were programmed into WaveProp and propagated through the turbulence model. Due to the randomness of the turbulence model, each propagation yielded different results. To verify that the propagations were working properly, 10000 propagations were performed and averaged. This was then compared to the turbulent degraded irradiance pattern outlined in Sec. 2.7. For simplicity, the propagation distance was set to 90km for each iteration. Figure 30 shows the comparison of the WaveProp model and theory. The models match as well as the simulation allowed. If the number of propagations were increased to infinity, the plots would match up perfectly. Listing A.3 in Appendix A shows the code used

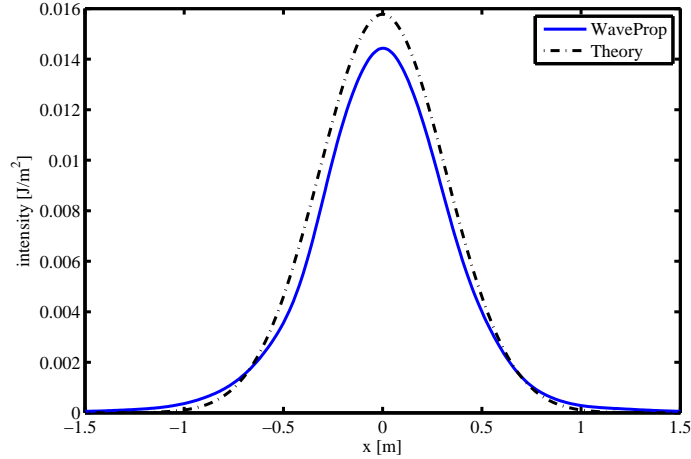


Figure 30. The center cutaway of the Gaussian beam turbulence propagation to the mean of the sodium layer (90km). The simulation result (blue) has the same trend as the theoretical expression (black).

to propagate and verify turbulence-degraded Gaussian beams. Now that our method to create an elongated beacon model has been verified, the next step is to view the beacon with the SHWFS lenslets to show perspective elongation. The next subsection explains how this was accomplished.

3.1.4 Simulating Perspective Elongation.

To simulate perspective elongation in SHWFS subapertures, the first step was to propagate the elongated beacon back through the atmosphere (sky to ground) to the telescope aperture plane. As a reminder, an actual telescope was not used since it has no direct effect on the elongation phenomenon. Instead, the SHWFS lenslets were placed in the primary telescope aperture plane.

The Fourier optics principles in Sec. 2.1 were exploited for all downward propagations. Instead of a complex shape, point sources were propagated through the entire optical system to obtain the PSF's in each subaperture. They were then convolved and averaged with the original objects to obtain the final image. The “objects” in this case were the irradiance patterns formed by the Gaussian beam propagation to

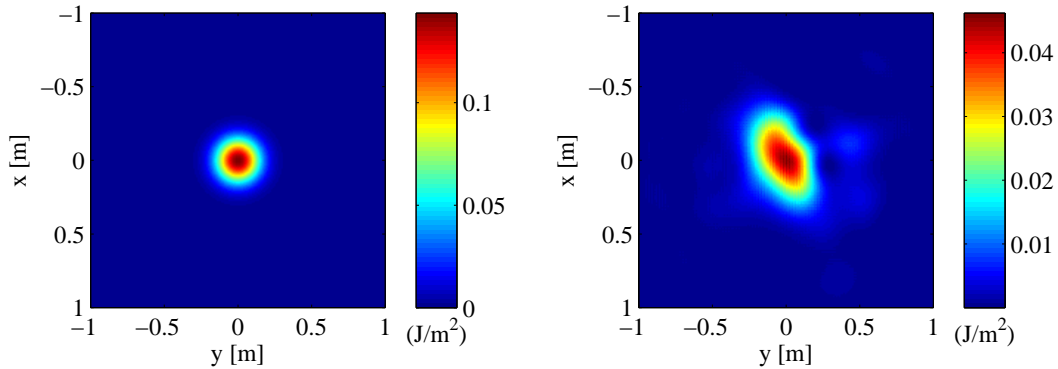


Figure 31. Gaussian beam irradiance pattern at central slice of the sodium layer (90km). Propagated through vacuum (left) and through turbulence (right).

different slices (distances) in the sodium layer (as discussed in the previous subsection). As an example, Fig. 31 shows the irradiance patterns through vacuum and turbulence of the center slice of the sodium layer (90km). It should be noted that the same turbulence draw was used in all propagations. Also, the tilt was removed from the turbulence beacon in the downward propagations. This can be seen in Fig. 31, where peak of the perturbed irradiance pattern is centered at the origin.

The number of point sources used corresponded to the number of slices the sodium layer was divided into. For example, in the seven slice scenario, a point source was propagated from each slice through the turbulent path and the optical system. The separation distance a between the LGS launching system and the SHWFS lenslets was modeled by shifting the point sources in each slice off the optical axis. Fixing the mean slice H_{Na} at 90km aligned with the optical axis, point sources were shifted in the x and y directions by:

$$x = a \left(\frac{H_S}{H_{Na}} - 1 \right) \quad (42)$$

$$y = a \left(\frac{H_S}{H_{Na}} - 1 \right), \quad (43)$$

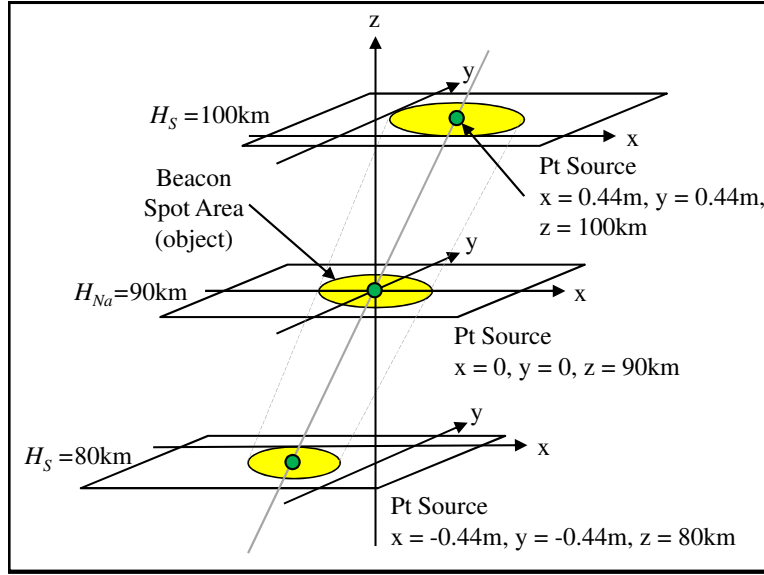


Figure 32. The point source coordinates determined by basic trigonometry. This figure only shows the coordinates for the point source in the top, middle, and bottom slices for simplicity.

Table 4. An example of the point source coordinates for the seven-slice scenario.

Slice	x [m]	y [m]	z [km]
1	-0.444	-0.444	80
2	-0.296	-0.296	83.333
3	-0.148	-0.148	86.667
4	0	0	90
5	0.148	0.148	93.333
6	0.296	0.296	96.667
7	0.444	0.444	100

where H_S is the height of a slice. These equations were derived from the basic geometric setup of the simulation. Figure 32 shows the geometry for point source separation, and Table 4 lists the point source coordinates for the seven-slice scenario.

After propagating the point sources through the optical system, PSF's were formed in each SHWFS subaperture. Before the PSF's were convolved with the original object, the object's phase was collimated by removing the spherical vacuum phase of the center slice from every other slice. This was done to make the SHWFS lenslets

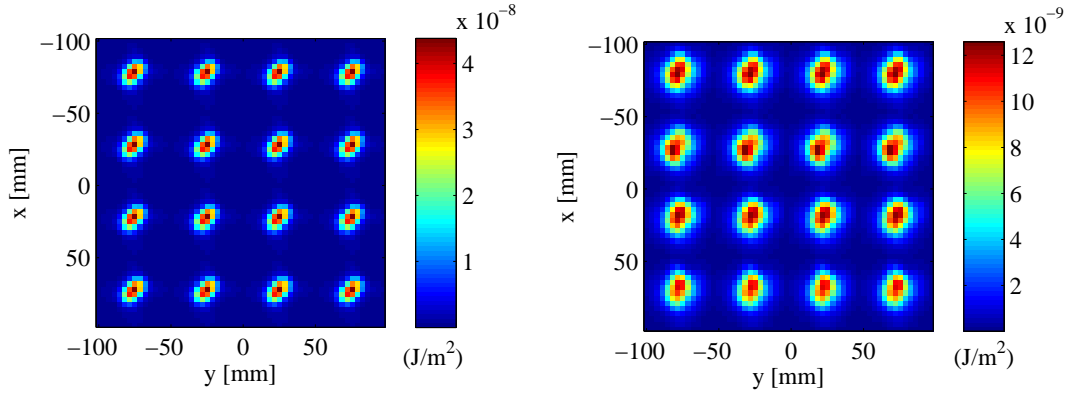


Figure 33. Elongated SHWFS spots formed from the seven slice model, (top) are spots through vacuum and (bottom) are spots through turbulence. This is a small sample (16 subapertures) of the entire SHWFS array (400 subapertures).

focused to the mean distance of the sodium layer (90km) since a telescope was not used. Finally, after the convolution was performed and averaged for each PSF and object from different sodium layer slices, the perspective elongation emerged. Propagations were done through both vacuum and turbulence conditions, and an example of the elongated spots in the SHWFS is displayed in Fig. 33. This figure shows the spots formed by the seven slice model, and only a small portion of the entire SHWFS array is displayed (16 subapertures).

The entire process was repeated to simulate perspective elongation using different numbers of sodium layer slices. The elongated spot images were compared by using RMS percent error and correlation coefficient. Listing A.4 in Appendix A displays the code used to simulate perspective elongation. The results are analyzed in Ch. IV. With a valid model for simulating perspective elongation in WaveProp, the next step was to experimentally create elongated spots in a SHWFS. The experimental methodology is discussed in the next section.

3.2 Laboratory Description

The purpose of this section is to introduce the AO lab bench-top setup used throughout this study. First, the operation of the AO system is discussed. Then, a ZEMAX model of the bench-top was then developed to determine the theoretical magnification and other characteristics of the system.

3.2.1 AFIT AO Lab.

The AO lab at AFIT contains all the components necessary to operate an AO system in the open- and closed-loop regimes. The system is capable of performing in moderate to strong turbulence, with Rytov numbers around 1. A diagram of the optical setup is shown in Fig. 34, and the components are listed in Table 5. The phase wheels and lenses L1-L7 make up the atmospheric turbulence simulator (ATS). The ATS is capable of producing a broad range of dynamic and static, low altitude and high altitude turbulence scenarios. A fiber-coupled laser diode, creating a near-point, is propagated through the ATS and reflected off the FSM. The FSM applies tip/tilt corrections to the collimated output beam based on commands made using centroid measurements from the tracker camera. After the FSM, the collimated beam enters a 4-f lens system composed of lenses L8 and L9. The 4-f system creates a conjugate pupil plane between the exit pupil of the ATS and the surface of the DM. The ratio of the focal lengths of lenses L8 and L9 applies proper magnification to shrink the beam to match the DM size. Reflection off the DM then applies higher-order aberration corrections based on commands made from gradient measurements using the SHWFS. The collimated light is then propagated through another 4-f system (with unit magnification) and a series of beam splitters and folding mirrors until it is captured by the tracker camera and the SHWFS. All optical components past the ATS comprise the AO system.

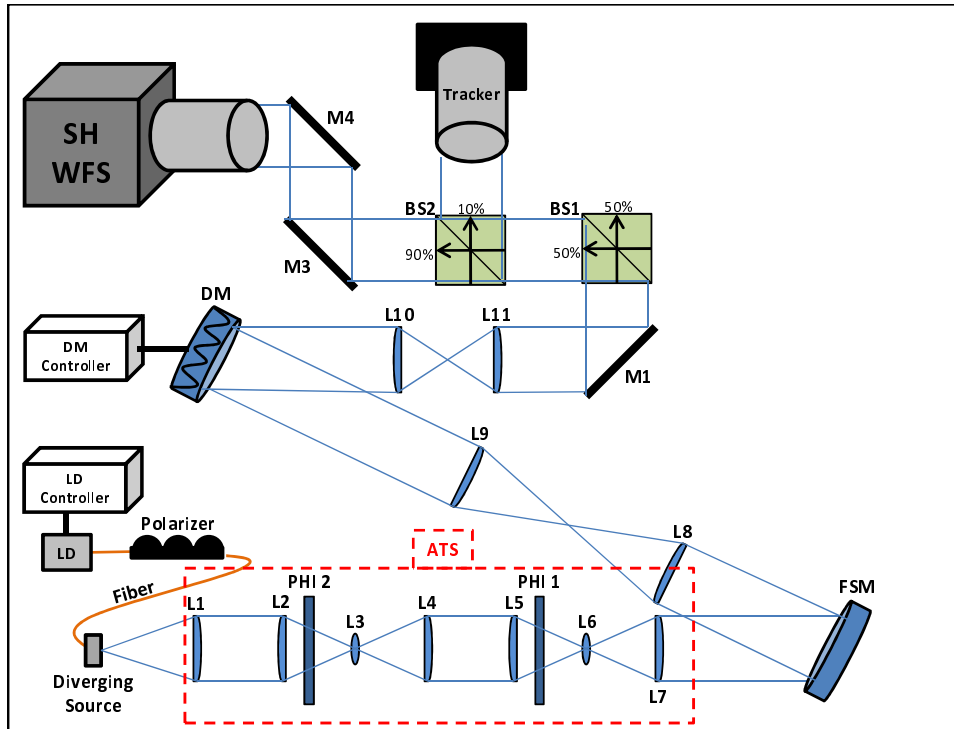


Figure 34. Physical layout of the turbulence simulator and AO system.

Table 5. Lab bench components

Symbol	component
LD	laser diode
L1-L11	lenses
PHI 1 and PHI 2	phase wheels
M1, M3, and M4	fold mirrors
BS1 and BS2	beam splitters
FSM	fast steering mirror
DM	deformable mirror
Tracker	tracking camera
SHWFS	Shack-Hartmann WFS

3.2.2 ZEMAX Model.

ZEMAX is a software program used for optical lens design and system layout. Each optical surface is logged in a spreadsheet using characteristics such as: radius of curvature, propagation distance, and propagation medium. A point source (on- or off-axis) can then be propagated through the optical layout using any number of geometric rays. For the purpose of this research, ZEMAX was used to model the bench-top setup to determine the location of the aperture stop, field stop and, ultimately, the magnification of the system. These details were important to scale the software-modeled, elongated beacon to the bench-top system.

The ZEMAX model of the system was simplified, including only the ATS, the 4-f relay, and a single lenslet of the SHWFS. Starting on the optical axis, a point source was first propagated through the model using rays. Incrementally, the point source was placed further off axis, and propagated through the model until an optical component began to clip the rays. The first optical component to vignette the rays was the lenslet while the rays were only completely stopped at the subapertures detector region. Thus, these components are the aperture stop and field stop, respectively. Figure 35 shows the 2D ZEMAX layout of the lab bench where the blue rays emanate from a point source on axis and the green rays emanate from a point source off axis. Since the system is very long when shown with a 1:1 aspect ratio, only the ATS and SHWFS lenslet are shown.

To find the theoretical transverse magnification M_T , rays from a point source separated a small distance S_o off the optical axis were traced through the system. These rays then converged to a point on the detector plane a small distance off the optical axis S_i . The theoretical transverse magnification M_T and longitudinal

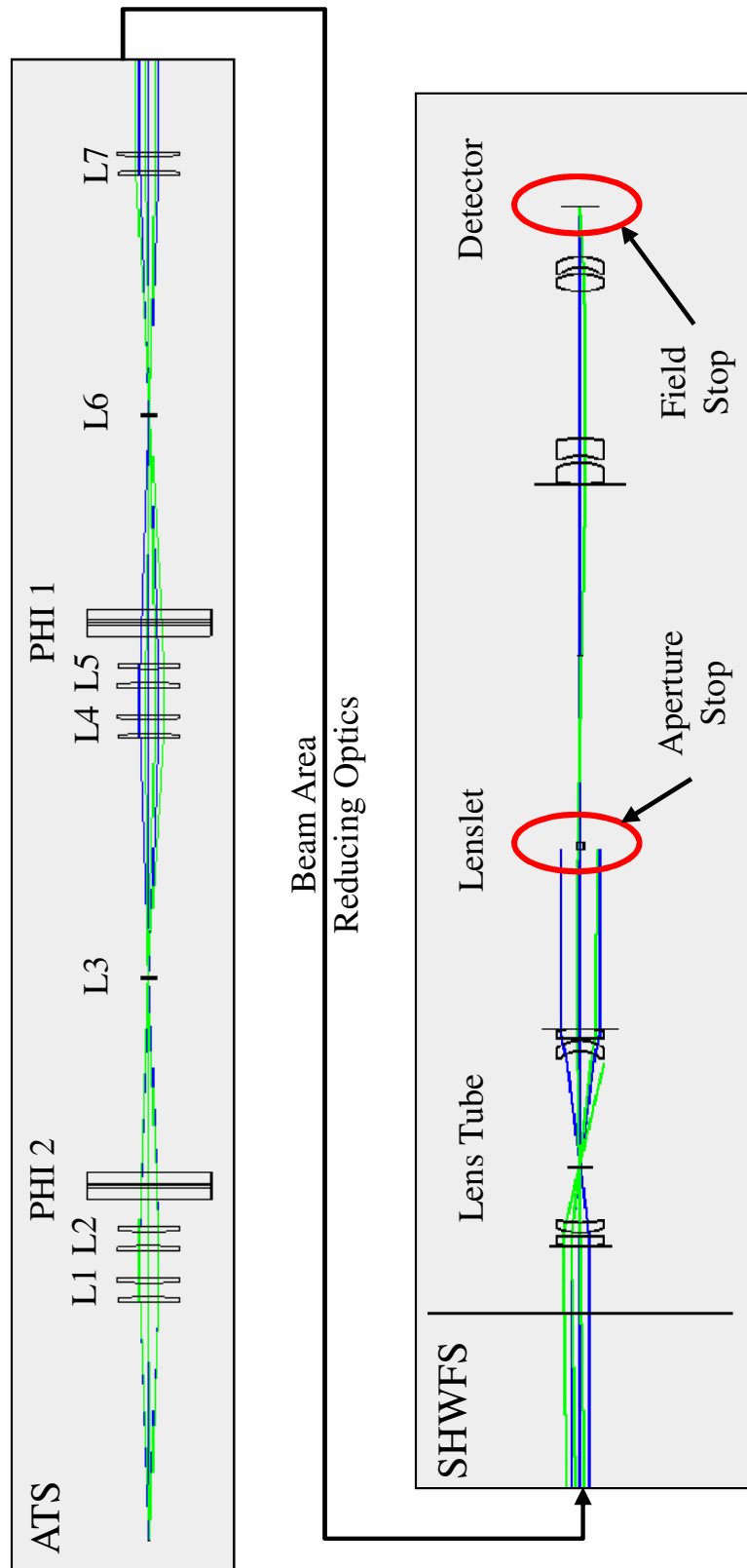


Figure 35. The ZEMAX model of the AFIT lab bench-top AO system. Only the ATS and SHWFS lenslet are displayed due to space constraints. The optical component labels are consistent with those in Table 5. The blue rays are from a point source on axis and the green lines are from a point source off axis. The field stop and aperture stop are circled in red. REDO PICTURE!!!

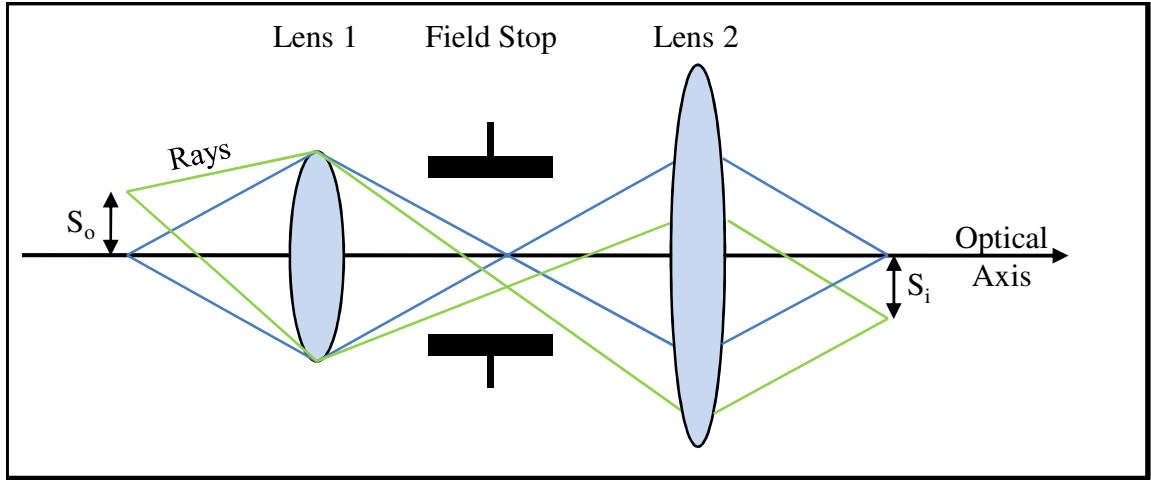


Figure 36. Determining system magnification by taking the ratio of image ray height S_i and source ray height S_o from the optical axis.

magnification M_L was calculated by[22]:

$$M_T = \frac{S_i}{S_o} \quad (44)$$

$$M_L = M_T^2. \quad (45)$$

Figure 36 shows a simplified picture of how to determine the theoretical magnification of an optical system. The magnification parameters M_T and M_L were found to be 0.13 and 0.0169, respectively. It should be noted that magnification determined by ZEMAX is only valid for images formed in the SHWFS. Lab experiments, discussed in the next section, were used to verify the ZEMAX magnification.

3.3 Extended Source Model Progression

Creating a three-dimensional scattering volume on the optical table was done in incremental steps. First, different optical components were arranged to create adjustable, extended 2D sources. The extended sources were propagated through the optical system and captured by the SHWFS and tracker camera. Proper measure-

ments were taken to determine the actual magnification of the system and verify the ZEMAX model. Finally, the source was tilted to produce source elongation and imaged by the system.

Due to the limitations of the bench-top system (2mW maximum laser power and fixed focal length of the ATS's collimating lens $L1$), determining the proper combination of optical elements to create an extended source was an iterative process. The main trade off was making the source diverge enough while still producing enough irradiance to be detected by the sensors. To do this, a method of using an iris and different diffusers is discussed in the next section.

3.3.1 Iris and Diffuser.

To create an adjustable extended source the 1550nm, 2mW laser diode was first attached to a small collimator and carefully aligned to the ATS's optical axis. The beam was then propagated through an adjustable iris placed at the front focal point of the first lens $L1$ in the AO system. The light departing the iris did not diverge wide enough to fill the full aperture of the SHWFS. To correct this, a motor-mounted diffuser was placed before the iris. Figure 37 shows a picture of the source setup. As discussed in Sec. 2.2, the spinning diffuser was necessary to reduce the spatial coherence in the beam. Figure 38 shows a comparison of the image with and without the diffuser spinning in the tracker camera. While speckle similarly affects both sensors, the tracker camera provides a higher-resolution image to depict the speckle and lack thereof.

Two collimators with different diameters (2mm and 7mm) and four different diffusers, each with a different grid designation (P120, P220, P600, and P1500), were available for setting up the source. The first experiments were done to determine which collimator/diffuser combination created the most adjustability while still per-

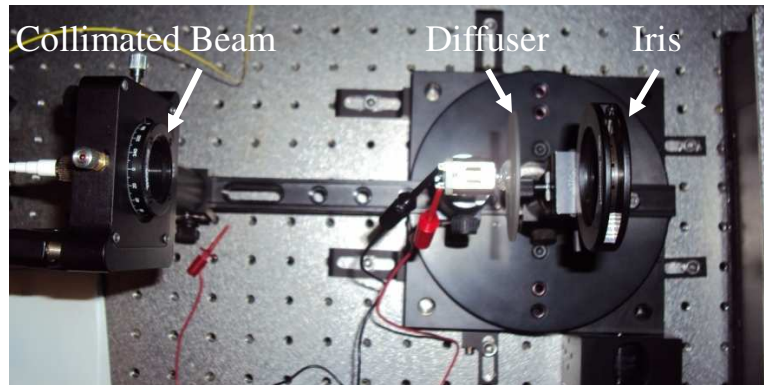


Figure 37. The collimated beam passes through the iris to create a diverging, incoherent source. The iris is then adjusted to the desired size.

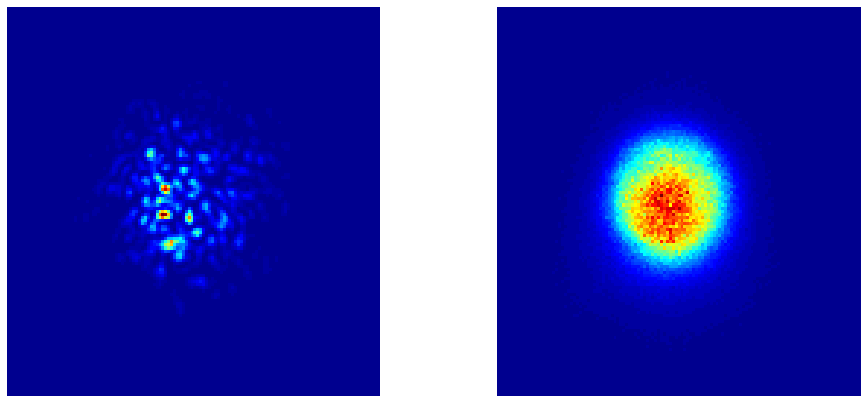


Figure 38. Effects of a diffuser on a collimated, coherent source. Image-plane speckle (left) is caused by a stationary diffuser and is averaged out by a rotating diffuser (right).

mitting enough irradiance to be captured by the sensors. Only one diffuser was used at a time due to their high attenuation. Two diffusers, no matter what grit, decreased the irradiance to undetectable levels in the sensors. Section 4.2 displays the results in a table and determines the best combination to use. It should be noted that the correct combination was determined qualitatively by observing the irradiance patterns in the sensors.

3.3.2 System Magnification.

To verify the magnification of the system, a simple experiment was done using the adjustable iris and spinning diffuser setup. The iris (object S_o) was set to 0.5mm and its image was captured by the SHWFS. It should be noted that the actual diameter of the source was approximately 1mm since S_o is defined as the distance from the optical axis to the edge of the object. Using a single subaperture, the illuminated pixels across the spot were counted and multiplied by the pixel pitch ($25\mu\text{m}$) to get the size of the image S_i . As in the ZEMAX calculation, the ratio of S_i to S_o was taken to determine the transverse magnification M_T . Figure 39 shows the SHWFS images formed by the 1mm source. The higher-resolution tracker could not be used for this calculation because the two sensors may have different fields of view, and the SHWFS is the primary concern here. The system magnification was determined to be approximately 0.15 (± 0.03 due to inaccuracies with measuring the iris diameter by hand and the pixel cut-off in the image). The experimental magnification matched closely to the ZEMAX-determined magnification of 0.14.

3.3.3 Three-Dimensional Extended Source.

Once the proper iris/diffuser combination and magnification of the system was determined, the next step was to produce extended-source properties. It is important

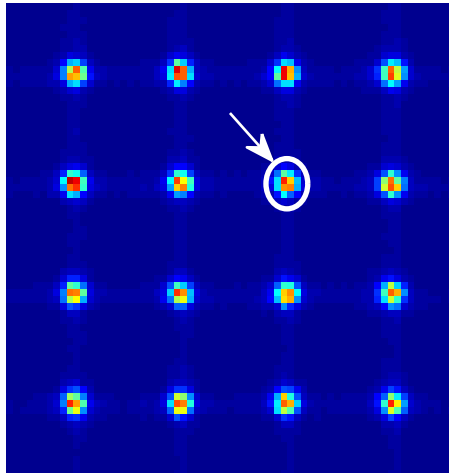


Figure 39. SHWFS spots formed by imaging a 1mm extended source. This is a small sample (16 subapertures) of the entire SHWFS array (81 subapertures). The pixels encompassed by the white circle were those used in the magnification calculation.

to mention that all extended sources modeled here were not formed by propagating light through random media as was done in the software simulations due to limitations with the bench-top setup. Here, the three-dimensional extended source was modeled by aligning the center of the iris with the optical axis and tilting it to different angles. Figure 40 shows a picture of the rotated iris. Applying the system magnification determined in the previous section, the beacon model must have a diameter of 1.5mm and a depth of approximately 8mm. These dimensions would theoretically create similar SHWFS image size and depth as those in the software simulations. Unfortunately, the physical limitations of the iris and its mechanical mount prevent it from achieving these dimensions.

Even though this model theoretically cannot recreate the exact SHWFS spots observed in the software simulations, it was still used to determine if spot elongation could be simulated this way, on this bench-top setup. The iris was set to 90° (perpendicular to the optical axis), 45° , and 30° , and imaged by the sensors. The hole of the iris in each scenario was adjusted so that a source width of 1.5mm of light was

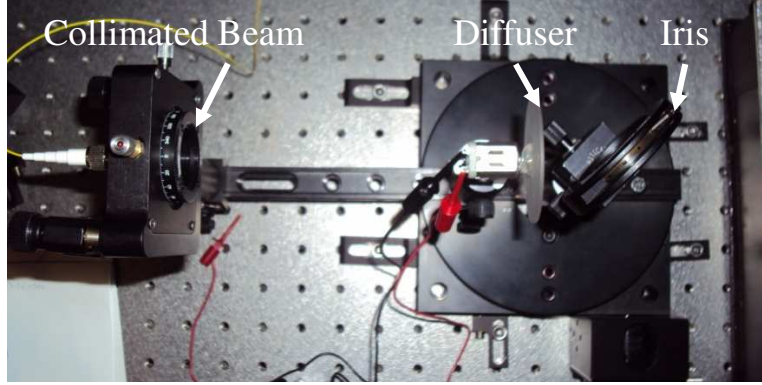


Figure 40. The collimated beam passes through the iris to create a diverging, incoherent source. The iris is then opened to adjust width and tilted to adjust beacon depth.

always visible to the system. This forced the iris to be opened more and more, which was necessary to let enough light through. Figure 41 shows a picture of the three different iris rotations and the subsequent increases in iris size. Each source rotation was propagated through vacuum and turbulence and imaged through the sensors with the AO loop closed. The turbulence was considered weak with a Rytov number of 0.02 and an r_0 of 0.77mm at the DM. With $d/r_0 = 0.65$, these conditions are similar to what was used in the computer simulations. The data is analyzed in Sec. 4.2. Due to manufacturing challenges and time constraints, other methods of modeling a three-dimensional extended source were not attempted. Several, more sophisticated methods are suggested in the Ch. V.

3.4 Data Collection and Comparison

For each source experiment, 100 frames from the tracker camera and 200 frames from the SHWFS were captured and analyzed. Since the diffusers significantly reduced the irradiance of the source, the exposure periods of the sensors were relatively long. Table 6 lists the sensor settings used to capture data in all experiments. Analysis was done via MATLAB by reading in the frames, averaging the frames, and temporally re-sampling the data. Re-sampling each set basically equalized the exposure

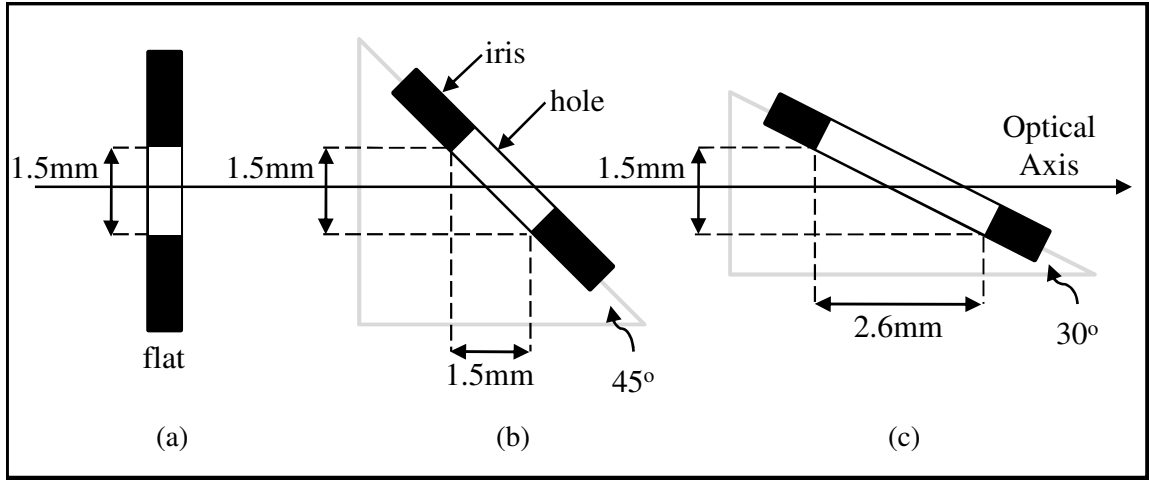


Figure 41. The rotation of the iris to form extended sources of different depths. The depth of the source increases as the angle decreases. In (a) the iris is set perpendicular to the optical axis, giving the source no depth. In (b) the iris is set 45° to the optical axis, giving the source a depth of 1.5mm. In (c) the iris is set 30° to the optical axis, giving the source a depth of 2.6mm.

Table 6. Sensor settings used to capture data in all lab experiments.

	Capture Length [s]	Number of Frames	Frame Rate [Hz]	Exposure Period [μ s]
Tracker	0.1979	102	515.4	500
SHWFS	0.2062	200	970	150

period so the data could be accurately compared.

3.5 Chapter Summary

In summary, software simulations were first used to verify a documented method for creating elongated beacon models in the sodium layer. These beacons were compared by analyzing the elongated spots they formed in SHWFS subapertures. Next, a ZEMAX model of the AO system was developed to determine the aperture stop, field stop, and magnification of the system. On the lab bench-top, a simple experiment was done to verify the magnification which ultimately determined the 3D source dimensions to use in the lab experiments. Next, an adjustable iris and spinning difusers were used on an AO lab bench-top to simulate perspective elongation in the

SHWFS. In chapter IV, simulated and experimental data are analyzed to determine sufficient methods of modeling perspective elongation.

IV. Results and Analysis

This chapter presents the results and analysis for the comparison of perspective elongation models developed in Ch. III. The results are organized into three sections. The first describes the best way (according to this study) to model perspective elongation with insight gained from the computer simulation results. The second section presents the results from different bench-top, extended-source experiments. Finally, the experimental results are compared with the computer simulation results.

4.1 Computer Simulation Results

Perspective elongation in SHWFS subapertures was simulated by modeling an elongated beacon in the sodium layer and propagating it through the AO system. The elongated beacon was modeled 19 ways by dividing it into different numbers of evenly-spaced slices. This created slightly different elongated spot images in each SHWFS subaperture. Comparing the spot images by using the techniques discussed in Sec. 2.9 determined the minimum number of slices needed to accurately model the elongated beacon.

4.1.1 RMS Percent Difference.

The first method of comparing the elongated spots was done by using the RMS percent difference. Figure 42 shows the RMS percent difference of spot shapes formed by adjacent, increasing numbers of slices in both vacuum and turbulence scenarios, using slices of constant and column-density-weighted intensity. In all cases, the spot shapes decrease in percent difference when formed by an increasing number of slices. As expected, the spots formed by column-density-weighted slices cause a smaller initial difference due to the relatively low intensity levels at the edges of the sodium

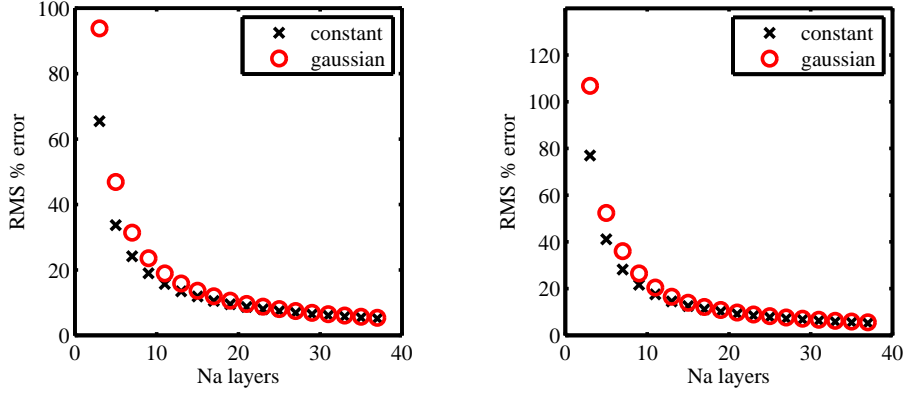


Figure 42. RMS percent difference comparison of elongated spots, (left) is the percent change in elongated spot shape formed through vacuum and (right) is the percent change in spots formed through turbulence. Black represents sodium layers at constant intensity and red represents layers with Gaussian weighting.

layer.

Even with a large number of slices, the percent difference never dropped below 8% which is too high to definitively determine how many slices are adequate. The relatively large difference is probably because this comparison technique compares exact data values instead of how correlated the different SH images are. Including another two slices of intensity data each simulation always increased the spot brightness in the SHWFS subapertures. Another comparison technique to that isolates the spot shapes with insensitivity to exact values.

4.1.2 Correlation Coefficient.

A more accurate way of comparing the change in spot shapes is by calculating the correlation coefficient between corresponding spot images. This essentially compares the two-dimensional flattened spot images formed by the different number of sodium layer slices. Using the 39 slice model as the “continuous” model, the correlation coefficient was calculated between it and the “discrete” models (3-37 slices). Figure 43 shows the plots of the correlation coefficient using slices of constant and column-density-weighted intensity.

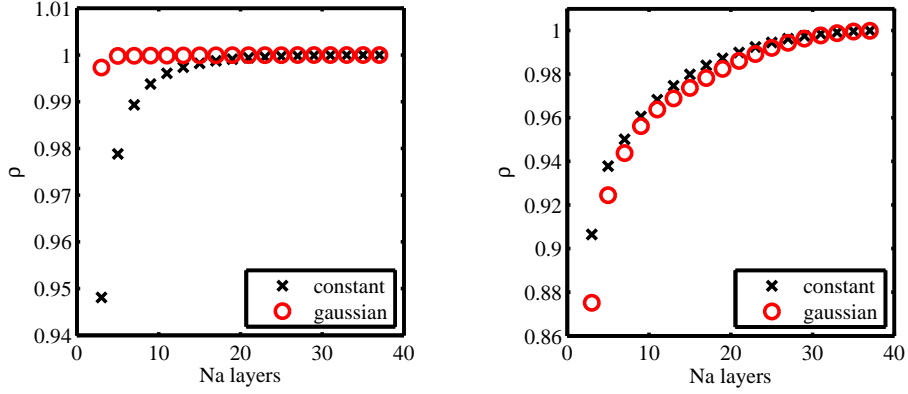


Figure 43. Correlation coefficient comparison of elongated spots, (left) are the coefficients for spots formed through vacuum, and (right) are the coefficients for spots formed through turbulence. Black represents sodium layers at constant intensity and red represents layers with Gaussian weighting.

As evident in the plot, the spot images in both vacuum and turbulence are highly correlated. If we consider 0.95 to be the correlation threshold, then the 3 slice elongated spot model is sufficient for the vacuum case. For the turbulence case, the 9 slice elongated spot model is sufficient. As a reminder, the elongated spots were formed using propagations near zenith. As the angle from zenith increases, the beacon elongates more. In these cases, more slices may be necessary to sufficiently model the elongated beacon.

4.2 Experimental Results

The experimental results and analysis are presented here. The proper diffuser and iris combination for our AO bench-top setup was determined first. With the proper combination, the iris was adjusted and rotated to create elongation in SHWFS subapertures. The subsections below provide all relevant details and imagery.

Table 7. The divergence and irradiance of different diffusers applied to two collimated 2mW beams.

beam diameter [mm]	diffuser grit classification							
	120		220		600		1500	
	div.	irrad.	div.	irrad.	div.	irrad.	div.	irrad.
2	good	good	good	good	poor	good	poor	good
7	good	poor	good	poor	poor	good	poor	good

4.2.1 Iris and Diffuser.

Pairing each diffuser with the adjustable iris, the divergence of the source and irradiance was observed by the tracker camera and SHWFS. Table 7 shows the performance of each diffuser using two different collimated beams. The only combination that produced a wide enough divergence angle and enough irradiance was the 2mm collimator paired with the coarsest diffusers (120 and 220). The 7mm beam would have provided the most flexibility in the source, but the power was too weak once it was spread that much. All other combinations either did not produce enough divergence or enough irradiance. All observations were qualitative. While this experiment did not provide any direct contribution to producing perspective elongation, it was a key step in the process and gives the boundaries for modeling an extended source on this lab bench-top. Ultimately the 2mm collimator with the 120 diffuser was chosen.

4.2.2 Three-Dimensional Extended Source.

Using the illuminated adjustable iris and diffuser as the source, the iris was rotated to three different positions to create three different extended sources. The first position was with the iris at 90° (flat), the second was with the iris at 45° , and the third was with the iris at 30° . The three source positions/shapes were captured by the tracker camera and the SHWFS after propagating through vacuum and turbulence. Figure 44 shows the sensor images through vacuum, and Fig. 45 shows the sensor

images through weak turbulence. As the angle of the iris decreased, the images in the sensors became more elliptical as was expected. In Figs. 44 and 45 the tracker image and corresponding SHWFS images are paired. The top pair of images (a) is with the iris at 90° , the middle pair (b) is with the iris at 45° , and the bottom pair (c) is with the iris at 30° . In the bottom pair of images, a larger region of interest (ROI) was needed to display the elongated beacon on the tracker. This makes the image seem smaller than the other two, but careful inspection of the dimensions show it is on the same order.

The vacuum and turbulence images are nearly indistinguishable. This is mainly because a small d/r_0 value (approximately 0.649) was used in the turbulence scenario. In this scenario, the spots did not show additional spreading, but did display a slight tilt. However, since all images were captured in the closed-loop regime, the tilt is not apparent in Fig. 45. A larger d/r_0 would most likely spread the spots much more and introduce more tilt, but this was not tested here and is outside the scope of this research. Additionally, while not part of the investigation, it was observed that the closed-loop Strehl ratio decreased with increasing spot size, as expected.

The SHWFS spots formed by the extended source model cannot be quantitatively verified with data from the software simulations. This is because the source dimensions to properly model the sodium beacon could not be achieved by just simply rotating the iris. During the course of the experiment, it was discovered that matching the depth of the beacon was outside the physical limitations of the simple iris. The exact iris dimensions would have been 1.5mm by 20mm, forcing it to be at a 4° angle with the optical axis. Ultimately, the narrow angle decreased the throughput of the beam so much that the source could not be imaged. More robust source designs must be developed in order to meet the required dimensions, and are outlined in Ch. 5. However, by doing the in-depth magnification experiments and calculations, the spots

are beginning to approach the sizes expected to be seen at SOR. Unfortunately, even a direct qualitative comparison cannot be accomplished for two reasons. First, SOR data was not releasable at the time of this research. Second, and more importantly, SOR uses a quad-cell based SHWFS and tracker. Essentially, each subaperture only consists of four pixels so information about spot shape is not captured, while the AO system in our lab has high-resolution subapertures and a full array tracker which has enough resolution to characterize the spot shape.

4.3 Chapter Summary

This chapter presented the results from both the software simulation of extended beacons and the lab experiments using extended sources. In all cases, the extended beacon models were evaluated by analyzing the spot shapes they formed in SHWFS subapertures. The software model showed that dividing the elongated beacon into 3 slices (for propagation through vacuum) and 9 slices (for propagation through turbulence) adequately modeled the elongated beacon in the sodium layer. This finding is consistent with claims made in current literature[5].

The bench-top extended source demonstrated preliminary steps toward modeling perspective elongation in a lab setting. By rotating and adjusting an iris illuminated incoherently by laser light passing through a moving diffuser, various levels of elongation were observed in SHWFS subapertures. It should be stressed that it is not clear if all properties of perspective elongation were created by the model, but the adjustable model is useful for many areas of future research as discussed in Ch. 5. While much more work needs to be done to accurately model perspective elongation on a lab bench-top, the experiments here will help pave the way by providing the first documented tests of extended sources on bench-top AO systems.

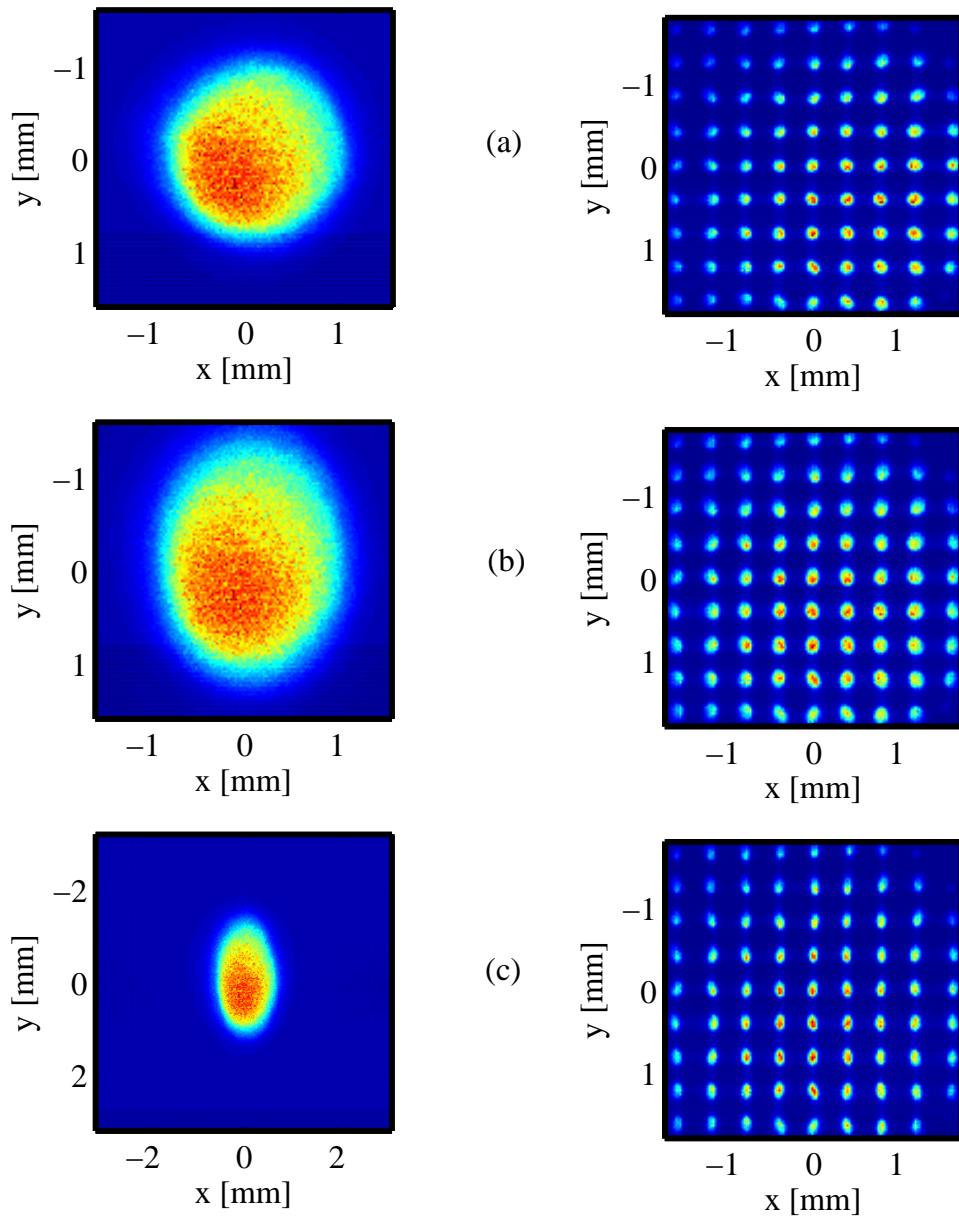


Figure 44. Extended source and resultant elongated SHWFS spots through vacuum. Starting with the top pair of images, (a) is with the iris set perpendicular to the optical axis (90°), (b) is with the iris set to 45° , and (c) is with the iris set to 30° .

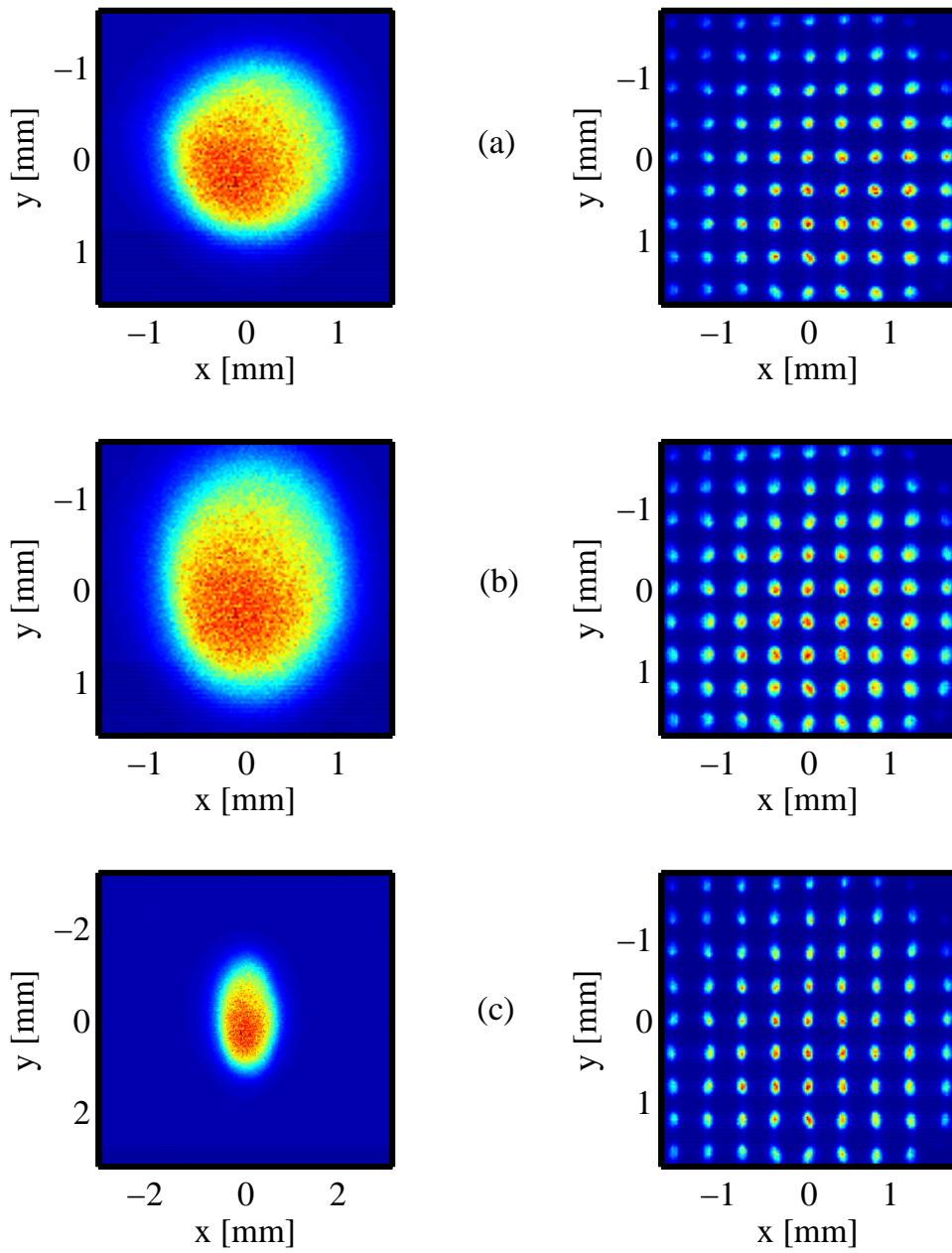


Figure 45. Extended source and resultant elongated SHWFS spots through turbulence. Starting with the top pair of images, (a) is with the iris set perpendicular to the optical axis (90°), (b) is with the iris set to 45° , and (c) is with the iris set to 30° . All images were captured in the closed-loop regime.

V. Conclusions and Recommendations

This chapter summarizes all pieces of this research. Key results from data analysis in Ch. IV are listed for easy reference. Additionally, recommendations for future work on perspective elongation are suggested.

5.1 Summary

As discussed in Ch. I, the objectives of this research were to validate a method for modeling an elongated beacon with wave propagation software, perform lab experiments to simulate perspective elongation in SHWFS subapertures, and deliver working, scalable software and lab models for simulating perspective elongation. Chapter II provided all the necessary background information used throughout the research. In Ch. III, software and lab environments were developed to meet Ch. I objectives. Using wave propagation software in MATLAB, an atmospheric turbulence model was developed. Gaussian beams were propagated through the model to the sodium layer to create an elongated beacon. Dividing the sodium layer into different slices created slightly different elongated beacon models. The models were analyzed by imaging them with a SHWFS and comparing the resultant elongated spots. The lab portion involved trying different methods of modeling an elongated scattering source to get elongated SHWFS spots. Two-dimensional sources were used to first determine the source width and a three-dimensional source was used to determine the source depth. Chapter IV analyzes the data from software and lab experiments. Data from the software model was used to verify the lab model. The next section summarizes the novel contributions from the software and lab experiments.

5.2 Novel Contributions

The novel contributions obtained in this study are:

- *Software model that recreates perspective elongation.* The software program effectively simulated the propagation of a sodium laser source to create an elongated beacon. The beacon was then imaged by a SHWFS to simulate elongated spots. Several parameters were adjustable such as: separation distance between the primary aperture and laser launching source, all propagation distances, turbulence strength, and SHWFS dimensions (number of lenslets, focal length, lenslet dimensions).
- *Number of slices needed to sufficiently model and elongated sodium beacon.* The number of slices to sufficiently model an elongate beacon was determined by analyzing the resulting SHWFS spots. In vacuum propagation, it was determined that only 3 slices were needed to accurately model the elongated beacon. In turbulence propagation, it was determined that at least 9 slices were needed.
- *Bench-top extended source model.* The bench-top source was created by propagating laser light through a moving diffuser and an adjustable iris. The moving diffuser was used to make the light spatially incoherent for imaging purposes. The iris was adjusted (opened and turned) to create the desired width and depth of the extended source.
- *Added capabilities to work with extended beacons.* While theorized about, the effects of extended beacons on WFS's have been widely untested. With the basic source setup used in this research, wavefront sensing with correlation-based slope measurements can be analyzed for different WFS such as the SHWFS and the Self-Referencing Interferometer (SRI). Additionally, the extended sources can be used to validate the effects of deep turbulence on AO systems[23][24][25].

Deep turbulence is essentially an extended source through strong turbulence. Strong turbulence has been well tested, but not when combined with an extended source. Thus, the model developed here adds the final piece to test deep turbulence theory.

5.3 Recommendations

This section provides recommendations for future work related to this research.

- *Elongated beacon software model.* The elongated spots used in the software simulation were modeled by dividing the sodium layer into slices. In each case, the slices were always equally spaced between 80 and 100km and centered at 90km. A better method may be to fix a slice at 90km and, keeping the distance constant, increase the number of slices equally above and below the center slice. Figure 46 shows a picture of this. This method may produce different results for the column-density-weighted scenario since the sodium atom concentration is greatest around 90km. For the constant weighted scenario, the results would be close if not exactly the same.
- *Telescope and atmospheric parameters in software simulations.* All software simulations were done modeling a 3.5m telescope pointed at zenith in relatively weak, static turbulence conditions. Changing any and/or all of these variable will definitely have an impact on the results. Assumedly, harsher conditions (larger telescope, angles from zenith, and stronger, dynamic turbulence) will need more slices to adequately model an elongated beacon.
- *Extended source lab models.* In this study, the bench-top extended source model was created by illuminating a rotated iris with incoherent light. While this created perspective elongation in the SHWFS subapertures, it had limits with

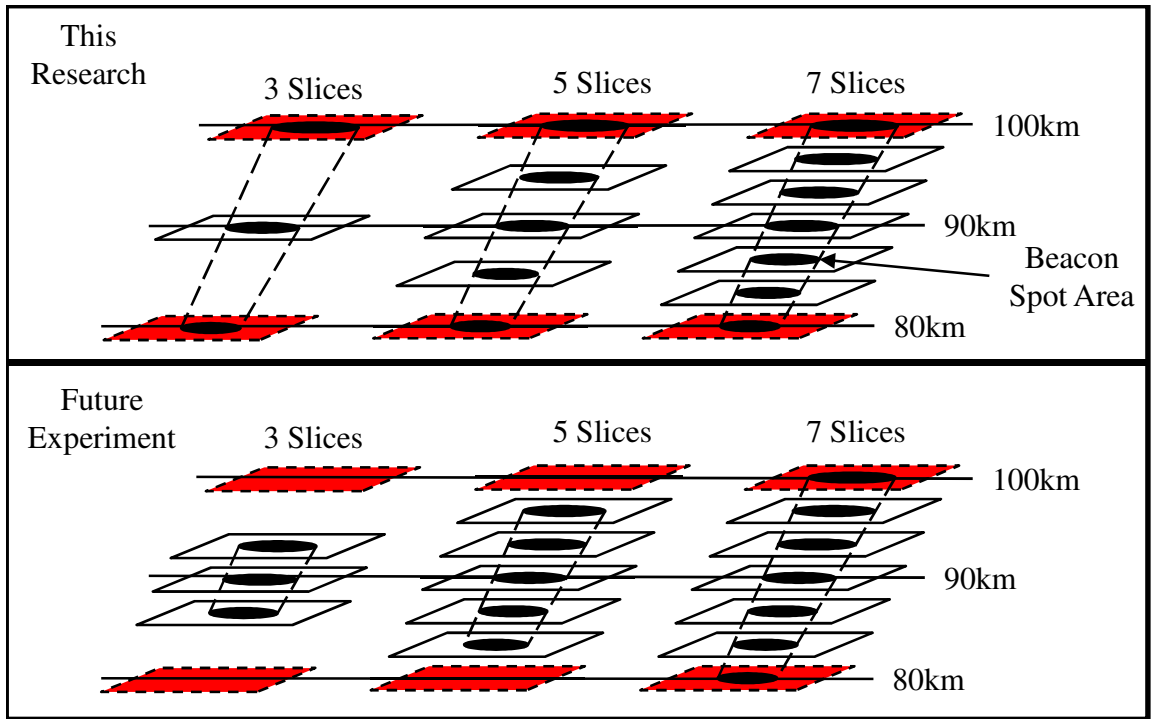


Figure 46. Two different ways of dividing the sodium layer to model elongated spots. The top figure shows the method used in this report and the bottom figure shows a possible future setup. A 3, 5, and 7 slice model is given for both setups.

changing the dimensions of the source. Three other ways to model a three-dimensional extended beacon are presented here.

The first model called the "rice grain" model involves using a highly reflective object roughly the size of a rice grain. Mounted on the rotating shaft of a motor and aligned with the optical axis, the grain would be illuminated by a coherent laser beam. Using the motor to rotate the grain would create an incoherent source to be imaged by the system. The rice grain could be rotated to any angle to create an extended three-dimensional source that matches the demagnified dimensions of an elongated sodium beacon. Figure 47(a) shows a picture of the "rice grain" model.

The second model called the "reflector tube" model is very similar to the "rice grain" model in that it uses a device mounted on a motor and aligned on the optical axis of the AO system. This source is made by injecting a clear resin mixed with highly reflective powder into a small glass tube. The device is then mounted on a motor shaft and illuminated by a laser. The tube could be rotated to any angle to create an extended three-dimensional source that matches the demagnified dimensions of an elongated sodium beacon. 47(b) shows a picture of the "reflector tube" model.

The third model called the "LED bar" model involves mounting several tiny light emitting diodes (LED)s on an adjustable, mechanical mount. Each diode would face the same direction, all pointed along the optical axis. The center of the bar would be positioned on the optical axis at the focus of the entrance pupil, and could be rotated to any position. Also, the width of the bar could be adjusted by expanding or contracting the device. Figure 48 shows a picture of the "LED bar" model.

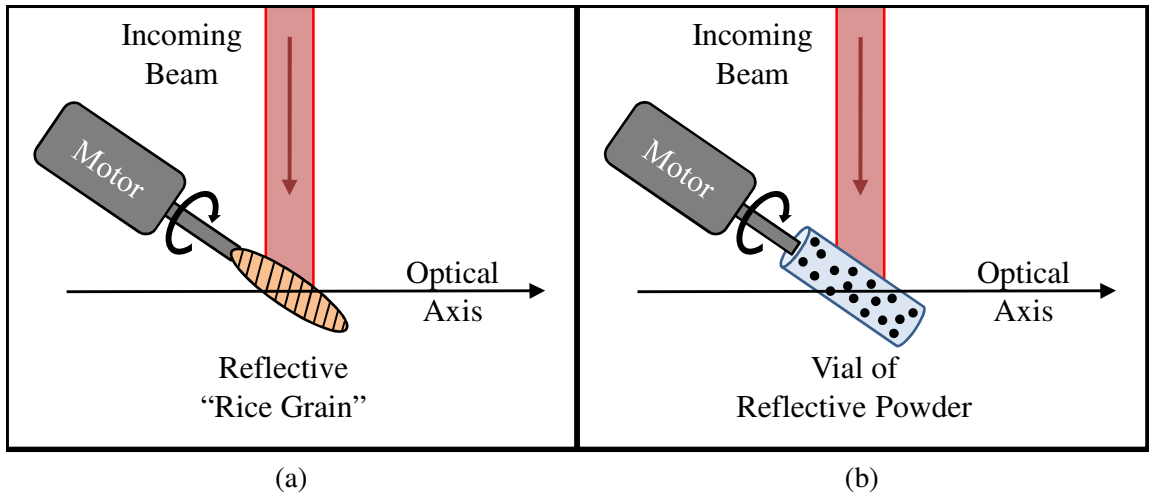


Figure 47. Two devices to possibly model an extended source. The rice grain (a) and the reflective tube (b) are both aligned with the optical axis and mounted on a motor. A laser is reflected off the spinning sources which could be rotated to any desired angle.

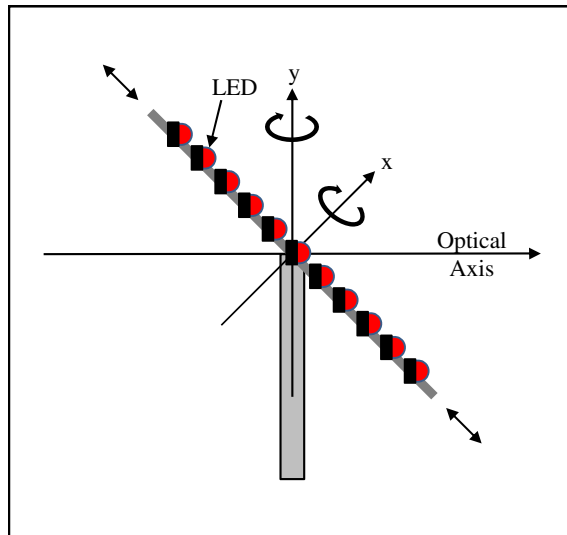


Figure 48. A deformable LED bar to possibly model an extended source. The bar could be expanded or contracted and rotated along any axis.

5.4 Chapter Summary

This chapter summarized the key results and presented some future research recommendations. The software model verified a documented beacon model to recreate perspective elongation, and the bench-top source model was a solid first step in simulating perspective elongation in the lab. Future recommendations included a different software model to simulation perspective elongation and a few different bench-top sources to better model an extended, three-dimensional source.

Appendix A. MATLAB Code

Listing A.1. LGS_Source.m

```
1 % Grid sampling parameters
2 N = 1024;% 512 number of grid points
3 Δn = 0.01; % 0.02 grid spacing in sodium layer [m]
4 Δl = 0.004; % 0.004 grid spacing in source plane [m]
5 L = N*Δn; % actual length of grid
6 wvl = 589.2e-9; % wavelength of sodium guidestar
7 k = 2*pi/wvl; % wave number
8 z = linspace(85e3, 95e3, nlayers); % propagation distance
9 % source parameters
10 W_0 = 0.08; % diameter
11 F_0 = 90000; % curvature
12 Theta_0 = 1-z/F_0; % focus
13 Lambda_0 = 2.*z/(k*W_0^2); % diffraction
14 % receiver parameters
15 W = W_0.*sqrt(Theta_0.^2 + Lambda_0.^2); % diameter
16 F = F_0*(Theta_0.^2+Lambda_0.^2).*(Theta_0-1)...
17     ./(Theta_0.^2+Lambda_0.^2-Theta_0); % curvature
18 Theta = Theta_0./(Theta_0.^2 + Lambda_0.^2); % focus
19 Lambda = Lambda_0./(Theta_0.^2 + Lambda_0.^2); % diffraction
20 % cartesian and polar coords (source plane)
21 [x1 y1] = meshgrid((-N/2 : N/2-1)*Δl); % grid
22 [Th1 r1] = cart2pol(x1,y1); % convert to polar coords
23 % Gaussian beam field and irradiance at source
24 U_gaus_s = exp(-(r1.^2)./(W_0^2)).*exp(-i*k.*(r1.^2)./(2*F_0));
25 I_gaus_s = abs(U_gaus_s).^2;
```

Listing A.2. LGS_Prop_Vac.m

```
1 % load vacuum ground to sky (g2s) model
2 load 'Turb_models'
3 z = linspace(80e3, 100e3, 7); % propagation distance (7 slices)
4 zm = mean(z); % middle Na layer
5 LGS_source % load Gaussian beam source parameters
```

```

6
7 % cartesian and polar coords (receiver plane)
8 [x2 y2] = meshgrid((-N/2 : N/2-1)*Δn); % grid
9 [Th2 r2] = cart2pol(x2,y2); % convert to polar coords
10
11 E_gaus = emfield(U_gaus_s, wvl, N*Δ1); % Make field for WaveProp
12 Vac_g2s.scaling=Δn/Δ1; % Proper vac scaling factor for WaveProp
13
14 % Propagate Gaussian field through vac/turb model
15 Ev_gaus_g2s = Vac_g2s(E_gaus);
16
17 z2 = z-50e3; % distance from 50km to 7 layers in mesosphere
18 layers = 7; % vac propagation to 7 slices in sodium layer
19 emarray_Na_v7 = zeros([N N layers]);
20 for idx=1:layers; % index for propagation distance
21     V2 = vacuum(z2(idx)); % propagate to the sodium layer
22     Ev_gaus_g2s_2 = V2(Ev_gaus_g2s); % WaveProp field thru vacuum
23     Iv_gaus = intensity(Ev_gaus_g2s_2); % WaveProp intensity thru vacuum
24     % Theoretical Gaussian beam field at receiver (from A&P)
25     U_gaus_r = 1./((Theta_0(idx)+i.*Lambda_0(idx)).*exp(i.*k.*z(idx)) ...
26         .*exp(-(r2.^2)./(W(idx).^2)).*exp(-i*k.*(r2.^2)./(2.*F(idx))));
27     % Theoretical Gaussian beam irradiance at receiver (from A&P)
28     I_gaus_r2 = abs(U_gaus_r).^2;
29 end

```

Listing A.3. Mean_Irradiance.m

```

1 %%%%%%%%%%%%%%%%%%%%%%%%%%%%%%%%%%%%%%%%%%%%%%%%%%%%%%%%%%%%%%%%%%%%%%%%%%
2 %% WaveProp models of Gaussian beam propagation thru Turbulence %%
3 %%%%%%%%%%%%%%%%%%%%%%%%%%%%%%%%%%%%%%%%%%%%%%%%%%%%%%%%%%%%%%%%%%%%%%%%%%
4 load 'Turb_models' % load turbulence model
5 Turb_g2s.proprange = 90e3; % set propagation distance in turb model
6 Turb_g2s.altitude2 = 90e3; % set altitude in turb model
7
8 z = 90e3; % constant propagation distance
9 LGS_source % load Gaussian beam source parameters
10
11 % cartesian and polar coords (receiver plane)

```

```

12 [x2 y2] = meshgrid((-N/2 : N/2-1)*Δn); % grid
13 [Th2 r2] = cart2pol(x2,y2);
14
15 E_gaus = emfield(U_gaus_s, wvl, N*Δ1); % Make field for WaveProp
16 Turb_g2s.scaling=Δn/Δ1; % Proper scaling factor for WaveProp
17
18 It_gaus_g2s_2 = zeros(N); % initialize variable in loop
19 props = 10000; % number of propagations
20 for idx = 1:props
21     Turb_g2s.seed = randi(10000); % change seed every prop
22     Et_gaus_g2s = Turb_g2s(E_gaus); % propagation thru turb model
23     It_gaus_g2s = intensity(Et_gaus_g2s); % intensity
24     It_gaus_g2s_2 = It_gaus_g2s_2 + It_gaus_g2s; % sum each irrad pattern
25 end
26 % WaveProp model of turb degraded irradiance (averaged)
27 I_gaus_turb = It_gaus_g2s_2/props;
28
29 %%%%%%%%%%%%%%%%%%%%%%%%%%%%%%%%%%%%%%%%%%%%%%%%%%%%%%%%%%%%%%%%%%%%%%%%%%
30 %%% Analytical Turbulence Degraded Irradiance %%%
31 %%%%%%%%%%%%%%%%%%%%%%%%%%%%%%%%%%%%%%%%%%%%%%%%%%%%%%%%%%%%%%%%%%%%%%%%%%
32 h=0:0.05:z; % Step size for integral
33 zen = 0*pi/180; % zenith angle [rad]
34 % HV-57 Cn2 Model
35 v=21; % velocity for HV57 [m/s]
36 A=1.7e-14; % Coefficient for HV57
37 Cn2 = 0.00594*(v/27)^2*(h*1e-5).^10.*exp(-h/1000)...
38     +2.7e-16*exp(-h/1500)+A*exp(-h/100);
39 %coherence length (spherical wave) to test
40 r0_down = (0.423*k^2*trapz(Cn2.*((z-h)./z).^ (5/3))...
41     *(h(2)-h(1))*sec(zen))^( -3/5)
42 % calculate variance factor
43 sigma2r = 8.3.*((Lambda(idx2)*z)/(k*r0_down^2))...
44     .^(5/6).*((r2.^2)./(W(idx2)^2));
45 % calculate T
46 T = 9.98*((Lambda(idx2)*z)/(k*r0_down^2)).^(5/6);
47 % analytical model of turb degraded irradiance (A&P page 189, Eqs. 45 & 46)
48 WLT = W(idx2)*sqrt(1+T);
49 I_gaus_turb_an = ((W_0^2)/(WLT^2)).*exp(-(2*r2.^2)./(WLT^2));

```

Listing A.4. Full_Propagation.m

```

1 %%%%%%%%%%%%%%%%%%%%%%%%%%%%%%%%%%%%%%%%%%%%%%%%%%%%%%%%%%%%%%%%%%%%%%%%%%
2 %%% Simulating Perspective Elongation in SHWFS Subapertures %%%
3 %%% 1. Beam propagation to sodium layer %%%
4 %%% 2. Beacon propagation to telescope from sodium layer %%%
5 %%% 3. Propagations done through both vacuum and turbulence %%%
6 %%%%%%%%%%%%%%%%%%%%%%%%%%%%%%%%%%%%%%%%%%%%%%%%%%%%%%%%%%%%%%%%%%%%%%%%%%
7
8 load 'Turb_models' %load vac and turb g2s/s2g models
9
10 vbase = 'Ivspots_nlayers_'; % base variable name for uncombined vac spots
11 tbase = 'Itspots_nlayers_'; % base variable name for uncombined turb spots
12 nlayers = [3,5,7,9,11,13,15,17,19,21,23,25,27,29,...
13           31,33,35,37,39]; % Na slices
14 Ispots_v = zeros([560 560 length(nlayers)]); % initialize spot turb vars
15 Ispots_t = zeros([560 560 length(nlayers)]); % initialize spot vac vars
16 for idxl = 1:length(nlayers); close all; % choose, loop over slice models
17     z = linspace(80e3, 100e3, nlayers(idxl)); % propagation distance
18     zm = mean(z); % middle Na layer
19     LGS_Source % calls gaussian beam source parameters
20
21     LGS_sep = 4; % LGS separation from center of tele ap [m]
22     tseed = 666; % constant turbulence seed for up & down props
23
24     [xn yn] = meshgrid((-N/2 : N/2-1)*Δn); % grid in receiver planes
25     [Thn rn] = cart2pol(xn,yn);
26
27 %%%%%%%%%%%%%%%%%%%%%%%%%%%%%%%%%%%%%%%%%%%%%%%%%%%%%%%%%%%%%%%%%%%%%%%%%%
28 %%% Propagate from ground to Na slices %%%
29 %%%%%%%%%%%%%%%%%%%%%%%%%%%%%%%%%%%%%%%%%%%%%%%%%%%%%%%%%%%%%%%%%%%%%%%%%%
30 E_gaus = emfield(U_gaus_s, wvl, N*Δ1); % make gaussian field for WP
31
32 Vac_g2s.scaling = Δn/Δ1; % proper scaling for WP
33 Turb_g2s.scaling = Δn/Δ1; % Proper scaling for WP
34 Turb_g2s.seed = tseed; % set the turb seed
35
36 Ev_gaus_g2s = Vac_g2s(E_gaus); % prop gauss fld 50km thru vac model
37 Et_gaus_g2s = Turb_g2s(E_gaus); % prop gauss fld 50km thru turb model
38
39 z_up = z-50e3; % distance from 50km to incremental NA slices

```



```

40 Iarray_Na_v = zeros([N N nlayers(idxl)]); % initialize vac up prop
41 Iarray_Na_t = zeros([N N nlayers(idxl)]); % initialize turb up prop
42 matlabpool; % initialize the matlab pool
43 for idx = 1:nlayers(idxl); % loop thru each slice;
44     V_up = vacuum(z_up(idx)); % set vac distance from 50km to slices
45     Ev_gaus_g2s_2 = V_up(Ev_gaus_g2s); % prop gauss beam thru vac
46     Et_gaus_g2s_2 = V_up(Et_gaus_g2s); % prop gauss beam thru turb
47     Iv_gaus = intensity(Ev_gaus_g2s_2); % find vac irradiance
48     It_gaus = intensity(Et_gaus_g2s_2); % find turb irradiance
49
50     % store layers (irradiance ONLY) in frames
51     Iarray_Na_v(:, :, idx) = [Iv_gaus.data];
52     Iarray_Na_t(:, :, idx) = [It_gaus.data];
53 end
54
55 %%%%%%%%%%%%%%%%%%%%%%%%%%%%%%%%%%%%%%%%%%%%%%%%%%%%%%%%%%%%%%%%%%%%%%%%%%
56 %%%% Propagate from Na slices to telescope aperture %%%%
57 %%%%%%%%%%%%%%%%%%%%%%%%%%%%%%%%%%%%%%%%%%%%%%%%%%%%%%%%%%%%%%%%%%%%%%%%%%
58 Δ50km = 0.0036; % grid spacing at 50km [m]
59 z_dn = z-50e3; % distance from levels in Na layer to 50km
60 [x50km y50km] = meshgrid((-N/2 : N/2-1)*Δ50km); % grid at 50km
61
62 % super gaussian (for filtering)
63 sigma = .15*L; n = 16;
64 SG_x = exp(-((x50km)/sigma).^n);
65 SG_y = exp(-((y50km)/sigma).^n);
66 SG_s = SG_x.*SG_y; % 3D square "gaussian"
67
68 Vac_s2g.scaling = Δn/Δ50km; % WP scaling at 50km
69 Turb_s2g.scaling = Δn/Δ50km; % WP scaling at 50km
70 Turb_s2g.seed = tseed; % set the turb seed (same as above)
71 emarray_ap_v = zeros([N N nlayers(idxl)]); % initialize vac down prop
72 emarray_ap_t = zeros([N N nlayers(idxl)]); % initialize turb down prop
73 for idx = 1:nlayers(idxl); % loop thru each slice;
74     xc = (z(idx)-zm)/(zm/LGS_sep); % sph wave x shift from op axis
75     yc = -(z(idx)-zm)/(zm/LGS_sep); % sph wave y shift from op axis
76
77     U_sph_an = (1./z_dn(idx)) ... % spherical wave equation
78         .*exp(1i*(k./(2.*z_dn(idx))).*((x50km-xc).^2+(y50km-yc).^2));
79     E_sph = emfield(U_sph_an, wvl, N*Δ50km); % make EM field for WP

```

```

80     E_sph = E_sph.*SG_s; % filter field with super gaussian
81
82     Ev_sph_s2g = Vac_s2g(E_sph); % prop sph wave through vac
83     Et_sph_s2g = Turb_s2g(E_sph); % prop sph wave through turb
84
85     % store fields at telescope aperture in frames
86     emarray_ap_v(:, :, idx) = [Ev_sph_s2g.data];
87     emarray_ap_t(:, :, idx) = [Et_sph_s2g.data];
88     end
89
90     %%%%%%%%%%%%%%%%%%%%%%%%%%%%%%%%%%%%%%%%%%%%%%%%%%%%%%%%%%%%%%%%%%%%%%%%%%
91     %%%%% Make lenslet array and subaps %%%%%
92     %%%%%%%%%%%%%%%%%%%%%%%%%%%%%%%%%%%%%%%%%%%%%%%%%%%%%%%%%%%%%%%%%%%%%%%%%%
93     nsubs = 40; % number of subaps per side (based on r0)
94     d = D/nsubs; % diameter of each lenslet , (based on r0)
95     npix = 16; % number of pixels per subap
96     dpix = d/npix; % diameter of each pixel in subap
97     foc = 0.125*(d*nsubs*dpix)/(2*wvl); % focal length of lenslets
98     Lllets = lensletelement(d, foc); % make lenslets in WP
99     V_Lllets = vacuum(foc); % prop distance from lenlets to detector
100
101     %%%%%%%%%%%%%%%%%%%%%%%%%%%%%%%%%%%%%%%%%%%%%%%%%%%%%%%%%%%%%%%%%%%%%%%%%%
102     %%%%% Make elongated spots %%%%%
103     %%%%%%%%%%%%%%%%%%%%%%%%%%%%%%%%%%%%%%%%%%%%%%%%%%%%%%%%%%%%%%%%%%%%%%%%%%
104     % cartesian coords for for tele ap
105     Nt = 200; % grid pts across tele ap
106     [xt yt] = meshgrid((-Nt/2 : Nt/2-1)*Δn); % grid
107
108     % field propagated from middle Na layer (convert back to emfield)
109     % for collimating the fields
110     mid = ceil((length(emarray_ap_v(1,1,:)))/2); % find middle frame
111     Ev_mid = emfield(emarray_ap_v(:, :, mid), wvl, L); % make into field
112     Ev_mid = cookiecut(Ev_mid, D); % cut out a window size of tele ap (2m)
113     Ev_mid_ph = phasor(Ev_mid); % keeps phase only
114
115     % grid spacing to increase resolution of field at tele ap
116     Δn2 = Δn/2;
117     Nt2 = Nt*2;
118     [xt2 yt2] = meshgrid((-Nt2/2:Nt2/2-1)*Δn2);
119

```

```

120 % grid spacing for demagnified field (field in Na layer)
121  $\Delta a = 0.05/200$ ;
122 [xa ya] = meshgrid((-200/2:200/2-1)* $\Delta a$ );
123 % grid spacing to decrease resolution of field in Na layer (for conv)
124  $\Delta b = 0.05/14$ ;
125 [xb yb] = meshgrid((-14/2:14/2-1)* $\Delta b$ );
126
127 Iv_final = zeros(560); % initialize final irradiance (vac)
128 It_final = zeros(560); % initialize final irradiance (turb)
129 for idx = 1:nlayers(idxl); % loop thru each slice;
130     %%% manipulate fields at tele ap (sky to ground prop)
131     Ev = emfield(emarray_ap_v(:, :, idx), wvl, L); % convert back to fld
132     Et = emfield(emarray_ap_t(:, :, idx), wvl, L); % convert back to fld
133     % cut out 2mx2m window
134     window_Ev = cookiecut(Ev,D); % vac
135     window_Et = cookiecut(Et,D); % turb
136     % collimate field at tele ap (mult by conj phase from mid layer)
137     Ev_col = window_Ev.*conj(Ev_mid_ph); % vac
138     Et_col = window_Et.*conj(Ev_mid_ph); %turb
139     % make tele ap field double resolution , convert back to field
140     Ev_col2 = interp2(xt, yt, Ev_col.data, xt2, yt2);
141     Ev_col2 = emfield(Ev_col2, wvl, D); % vac
142     Et_col2 = interp2(xt, yt, Et_col.data, xt2, yt2);
143     Et_col2 = emfield(Et_col2, wvl, D); % turb
144     % propagate fields through lenslets to detector plane
145     Ev_CCD = V_Llets(Llets(Ev_col2)); % vac field at detectors
146     Et_CCD = V_Llets(Llets(Et_col2)); % turb field at detectors
147     Iv_CCD = intensity(Ev_CCD); % intensity only (vac)
148     It_CCD = intensity(Et_CCD); % intensity only (turb)
149
150     %%% manipulate fields in Na layer (ground to sky prop)
151     It_Na = Iarray_Na_t(:, :, idx); % simple rename for bookkeeping
152     % find location of max intensity (centroid)
153     yloc = -round(sum(sum(It_Na).*([-N/2 : N/2-1])...
154         /sum(sum(It_Na)))); % x separation
155     xloc = -round(sum(sum(It_Na,2).*transpose([-N/2 : N/2-1])...
156         /sum(sum(It_Na)))); % y separation
157     It_Na = circshift(It_Na,[xloc yloc]); % center max intensity
158     It_Na = emfield(It_Na, wvl, L); % convert to field, irrad already
159     Iv_Na = emfield(Iarray_Na_v(:, :, idx), wvl, L); % irradiance only

```

```

160 %cut out 2mx2m window of the field
161 window_Iv_Na = cookiecut(Iv_Na,D); % vac
162 window_It_Na = cookiecut(It_Na,D); % turb
163 % demagnify fields from Na layer
164 Iv_Na_dmag = magnify(window_Iv_Na, 0.025); % vac
165 It_Na_dmag = magnify(window_It_Na, 0.025); % turb
166 % interpolate demagnified field to 14 x 14 pixels
167 Iv_Na_conv = interp2(xa, ya, Iv_Na_dmag.data, xb, yb); % vac
168 It_Na_conv = interp2(xa, ya, It_Na_dmag.data, xb, yb); % turb
169
170 %%%% convolution to make elongated spots %%%%
171 temp_hor_v2 = zeros(1,14)'; % initialize horizontal temp variable
172 temp_hor_t2 = zeros(1,14)';
173 temp_ver_v2 = zeros(1,561); % initialize vertical temp variable
174 temp_ver_t2 = zeros(1,561);
175 for idx2 = 1:40; % horizontal index for 40 14x14 pixel subaps
176     for idx3 = 1:40; % vertical index for 40 subaps
177         % pull out each subap from array
178         temp_hor_v = ...
179             Iv_CCD.data(idx*14-13:idx*14,idx2*14-13:idx2*14);
180         temp_hor_t = ...
181             It_CCD.data(idx*14-13:idx*14,idx2*14-13:idx2*14);
182         % find max value of each subap
183         max_temp_hor_v = max(max(temp_hor_v)); % vac
184         max_temp_hor_t = max(max(temp_hor_t)); % turb
185         % normalize each PSF = PDF (divide by area in each subap);
186         temp_hor_v_norm = temp_hor_v/sum(sum(temp_hor_v)); % vac
187         temp_hor_t_norm = temp_hor_t/sum(sum(temp_hor_t)); % turb
188         % convolve PSF with pattern in sodium layer
189         temp_hor_v_c = max_temp_hor_v ...
190             *convn(temp_hor_v_norm,Iv_Na_conv,'same');
191         temp_hor_t_c = max_temp_hor_t ...
192             *convn(temp_hor_t_norm,It_Na_conv,'same');
193         %store convolved patterns horizontally
194         temp_hor_v2 = [temp_hor_v2, temp_hor_v_c]; % vac
195         temp_hor_t2 = [temp_hor_t2, temp_hor_t_c]; % turb
196     end
197 % store each row of subaps vertically
198 temp_ver_v2 = [temp_ver_v2; temp_hor_v2]; % vac
199 temp_ver_t2 = [temp_ver_t2; temp_hor_t2]; % turb

```

```

200         temp_hor_v2 = zeros(1,14)'; % reset variable (vac)
201         temp_hor_t2 = zeros(1,14)'; % reset variable (turb)
202     end
203     % remove initialized zeros
204     temp_ver_v2 =... % vac
205         temp_ver_v2(2:length(temp_ver_v2),2:length(temp_ver_v2));
206     temp_ver_t2 =... % turb
207         temp_ver_t2(2:length(temp_ver_t2),2:length(temp_ver_t2));
208     % add the spot locations
209     Iv_final = Iv_final + temp_ver_v2; % vac
210     It_final = It_final + temp_ver_t2; % turb
211 end
212 end

```

Bibliography

- [1] Hart, M., “Recent advances in astronomical adaptive optics,” *Appl. Opt.* **49**(16) (2010).
- [2] Sandler, D. G., [*Adaptive Optics in Astronomy*], ch. 11-13, Cambridge University Press (1999).
- [3] Beckers, J. M., Owner-Petersen, M., and Andersen, T., “A rapid refocussing system for the Euro50 telescope aimed at removing the perspective elongation of laser beacons,” *SPIE Proc.* **5169** (2003).
- [4] Vitayaudom, K. P., Sanchez, D. J., Oesch, D. W., Kelly, P. R., Tewksbury-Christle, C. M., and Smith, J. C., “Experimental analysis of perspective elongation effects using a laser guide star in an adaptive-optics system,” *SPIE Proc.* **7466** (2009).
- [5] Viard, E., Delplancka, F., Hubin, N., and Ageorges, N., “LGS Na-spot elongation and Rayleigh scattering effects on Shack-Hartmann wavefront sensor performances,” *SPIE Proc.* **3762**(8) (1999).
- [6] Hardy, J. W., [*Adaptive Optics for Astronomical Telescopes*], Oxford University Press, New York, NY (1998).
- [7] Goodman, J. W., [*Introduction to Fourier Optics*], Roberts and Company, Inc., Greenwood Village, CO (2005).
- [8] Goodman, J. W., [*Statistical Optics*], John Wiley And Sons, Inc. (2000).
- [9] Goodman, J. W., [*Speckle Phenomena in Optics: Theory and Applications*], Roberts and Company, Inc., Greenwood Village, CO (2006).
- [10] Schmidt, J. D., [*Numerical Simulation of Optical Wave Propagation*], SPIE Press, Bellingham, WA (2010).
- [11] Tyson, R. K. and Frazier, B. W., [*Field Guide to Adaptive Optics*], SPIE Press, Bellingham, WA (2004).
- [12] Andrews, L. C. and Phillips, R. L., [*Laser Beam Propagation through Random Media*], SPIE Press, Bellingham, WA, 2nd ed. (2005).
- [13] Sasiela, R. J., [*Electromagnetic Wave Propagation in Turbulence, Evaluation and Application of Mellin Transforms*], SPIE Press, Bellingham, WA, 2nd ed. (2007).
- [14] “Starfire optical range website.” <http://www.de.afrl.af.mil/SOR/index.htm> (2010).

- [15] Spinhirne, J., Allen, J., Ameer, G., Brown, J., Christou, J., Duncan, T., Eager, R., Ealey, M., Ellerbroek, B., Fugate, R., Jones, G., Kuhns, R. M., Lee, D., Lowrey, W., Olikier, M., Ruane, R., Swindle, D., Voas, J., Wild, W., Wilson, K., and Wynia, J., “Starfire Optical Range 3.5m adaptive optical system,” *SPIE Proc.* **3353** (1998).
- [16] Schwiegerling, J. and Neal, D., “Historical development of the Shack-Hartmann wavefront sensor,” tech. rep.
- [17] Platt, B. C. and Shack, R., “History and principles of Shack-Hartmann wavefront sensing,” *J. Ref. Sur.* **17** (2001).
- [18] Geary, J. M., [*Introduction to Wavefront Sensors*], vol. TT18, SPIE Press, Bellingham, WA (1995).
- [19] Drummond, J. D., Novotny, S., Denman, C., Hillman, P., Telle, J., Moore, G., Eickhoff, M., and Fugate, R., “Sodium guidestar radiometry results from the SOR’s 50W faser,” *AMOS Tech. Conf.* (2006).
- [20] Drummond, J. D., Novotny, S., Denman, C., Hillman, P., Telle, J., Moore, G., Eickhoff, M., and Fugate, R., “Sodium guidestar radiometry results from the SOR’s 50W faser,” *AMOS Tech. Conf.* (2007).
- [21] Kibblewhite, E. J., [*Laser Guide Star Adaptive Optics for Astronomers*], vol. 551 of *C*, ch. 3, Kluwer Academic Publishers, Dordrecht, The Netherlands (2000).
- [22] Hecht, E., [*Optics*], Pearson Education (2002).
- [23] Belen’kii, M. S., Barchers, J., Berg, E., Bruns, D., Fung, D., Gallant, R., Kirk, C., Runyeon, H., Rye, V., and Voass, J., “Laboratory demonstration of wavefront based stochastic parallel gradient descent adaptive optics system,” *SPIE Proc.* **6708** (2007).
- [24] Sergeyev, A. V., Piatrou, P., and Roggemann, M. C., “Bootstrap beacon creation for overcoming the effects of beacon anisoplanatism in a laser beam projection system,” *Appl. Opt.* **47** (2009).
- [25] Tyler, G. A., “Adaptive optics compensation for propagation through deep turbulence: initial investigation of gradient descent tomography,” *J. Opt. Sct. Am. A* **23**(8) (2006).

Vita

Captain Jeffery S Dennison received a BSEE from Kansas State University in 2006. He is currently working towards a MSEE in Directed Energy/Beam Control at the Air Force Institute of Technology (AFIT) with a completion date of March 2011. Capt Dennison is also a member of Eta Kappa Nu (HKN) honor society and the International Society for Optical Engineering (SPIE). Previous areas of work includes intelligence operations at the National Air and Space Intelligence Center (NASIC) and at the Combined Air Operations Center (CAOC) at Al-Udeid Air Base.

REPORT DOCUMENTATION PAGE

Form Approved
OMB No. 0704-0188

The public reporting burden for this collection of information is estimated to average 1 hour per response, including the time for reviewing instructions, searching existing data sources, gathering and maintaining the data needed, and completing and reviewing the collection of information. Send comments regarding this burden estimate or any other aspect of this collection of information, including suggestions for reducing this burden to Department of Defense, Washington Headquarters Services, Directorate for Information Operations and Reports (0704-0188), 1215 Jefferson Davis Highway, Suite 1204, Arlington, VA 22202-4302. Respondents should be aware that notwithstanding any other provision of law, no person shall be subject to any penalty for failing to comply with a collection of information if it does not display a currently valid OMB control number. **PLEASE DO NOT RETURN YOUR FORM TO THE ABOVE ADDRESS.**

1. REPORT DATE (DD-MM-YYYY) 24-03-2011		2. REPORT TYPE Master's Thesis		3. DATES COVERED (From — To) Aug 2009 — Mar 2011	
4. TITLE AND SUBTITLE SIMULATING THE EFFECTS OF AN EXTENDED SOURCE ON THE SHACK-HARTMANN WAVEFRONT SENSOR THROUGH TURBULENCE				5a. CONTRACT NUMBER	
				5b. GRANT NUMBER F2KBAC0006G001	
				5c. PROGRAM ELEMENT NUMBER	
6. AUTHOR(S) Jeffery S. Dennison, Capt, USAF				5d. PROJECT NUMBER ENGJON163	
				5e. TASK NUMBER	
				5f. WORK UNIT NUMBER	
7. PERFORMING ORGANIZATION NAME(S) AND ADDRESS(ES) Air Force Institute of Technology Graduate School of Engineering and Management (AFIT/EN) 2950 Hobson Way WPAFB OH 45433-7765				8. PERFORMING ORGANIZATION REPORT NUMBER AFIT/GE/ENG/11-08	
9. SPONSORING / MONITORING AGENCY NAME(S) AND ADDRESS(ES) Air Force Research Laboratory Darryl J. Sanchez, PhD 3550 Aberdeen Ave SE Kirtland AFB, NM 87117-5776 (505) 846-7209 (DSN:246-7209),email: darryl.sanchez@kirtland.af.mil				10. SPONSOR/MONITOR'S ACRONYM(S) AFRL/RDS	
11. SPONSOR/MONITOR'S REPORT NUMBER(S)				12. DISTRIBUTION / AVAILABILITY STATEMENT APPROVED FOR PUBLIC RELEASE; DISTRIBUTION UNLIMITED.	
14. ABSTRACT Perspective elongation in Shack-Hartmann wavefront sensor (SHWFS) spots is a phenomenon caused by an extended three-dimensional scattering beacon in the mesosphere (80-100km). Elongated spots cause errors in wavefront sensor measurements, which leads to poor turbulence compensation and decreased image resolution of the optical system. In order to compensate for elongated spots, a proper beacon model must be developed to simulate the error. In this paper, a documented theory for modeling an elongated sodium beacon and elongated SHWFS spots using sodium layer "slices" was tested. It was found that nine evenly-spaced slices were adequate to model the elongated beacon in the most stringent, turbulence-included case. Furthermore bench-top source was developed and tested to model SHWFS spot elongation in the lab. The source demonstrated the principle, but requires a more robust design to simulate sodium layer depth. Being the first documented experiment using an extended source on an adaptive optics (AO) system, it opens the door for more research to include: the effects of deep turbulence on AO systems and correlation based wavefront sensing with extended sources.					
15. SUBJECT TERMS adaptive optics, Shack-Hartmann wavefront sensor, perspective elongation, sodium laser guidestar, beacon, turbulence					
16. SECURITY CLASSIFICATION OF:			17. LIMITATION OF ABSTRACT UU	18. NUMBER OF PAGES 104	19a. NAME OF RESPONSIBLE PERSON Jason D. Schmidt, Maj USAF (ENG)
a. REPORT U	b. ABSTRACT U	c. THIS PAGE U			19b. TELEPHONE NUMBER (include area code) (937) 255-3636, x7224; jason.schmidt@afit.edu